Polar lows and their effects on sea ice and the upper ocean in the Iceland, Greenland and Labrador Seas

O. Gutjahr[1], C. Mehlmann[2]

[1]Max Planck Institute for Meteorology, Hamburg, Germany
[2]Otto-von-Guericke University, Magdeburg, Germany

Key Points:

- First explicit simulation of polar lows in a globally coupled climate simulation with kilometer-scale (2.5 km) resolution in all components
- Polar lows lead to considerable heat loss from the ocean near the sea ice edge and from leads and polynyas in the sea ice cover
- Polar lows are important for water mass transformation in the western Iceland and Greenland Seas and within polynyas

Corresponding author: Oliver Gutjahr, `oliver.gutjahr@mpimet.mpg.de`

Abstract

Based on two case studies, we show for the first time that explicitly resolving polar lows in a global climate model (ICON-Sapphire) with a high resolution of 2.5 km in all components (atmosphere, ocean, sea ice and land) leads to strong heat loss from the ocean near the sea ice edge and from leads and polynyas in the ice cover. Heat losses during marine cold air outbreaks triggered by polar lows lead to the formation of dense water in the Iceland and Greenland Seas that replenishes the climatically important Denmark Strait Overflow Water (DSOW). Further heat losses and the rejection of brine during ice formation in polynyas, such as the Sirius Water Polynya in northeast Greenland, contribute to the formation of dense water over the Greenland shelf. In the Labrador Sea, polar lows intensify cold air outbreaks from the sea ice and quickly deepen the ocean mixed layer by 100 m within two days. If mesoscale polar lows and kinematic features in the sea ice are not resolved in global climate models, heat loss and dense water formation in (sub-)polar regions will be underestimated.

Plain Language Summary

We show for the first time that resolving polar lows (strong strongs over polar oceans) in a global climate model called ICON-Sapphire, which has a high resolution of 2.5 km in all of its components (atmosphere, ocean, sea ice and land), leads to strong heat loss from the ocean near the sea ice edge and from leads and polynyas, which are open water areas in an otherwise closed ice cover. Heat loss and salt rejection during ice formation may contribute to dense water formation along the sea ice margin and in polynyas above the shelf. If these polar lows and open water areas in the sea ice cover are not resolved in global climate models, heat loss and dense water formation in (sub)polar regions will be underestimated.

1 Introduction

Polar lows (PLs) are the most intense cyclones of the polar mesoscale cyclone family, with subsynoptic scales of less than 1000 km (Orlanski, 1975) and near-surface wind speeds of more than 15 $\mathrm{m\,s^{-1}}$ that can reach hurricane force ($\geq 33\,\mathrm{m\,s^{-1}}$), forming over high-latitude maritime environments poleward of the polar front (Heinemann & Claud, 1997). Although short-lived weather phenomena, they pose a hazard to shipping, air traffic, and offshore installations due to high wind speed, icing, high waves, poor visibility, and heavy snowfall. The effects of PLs on local weather have been studied since the 1980s using uncoupled regional atmospheric models. However, their effects on climate and the ocean are less well understood (Moreno-Ibáñez et al., 2021). In a first step, we aim to study the effects of PLs on sea ice and the upper ocean in a global coupled kilometer-scale (2.5 km) climate model, analyzing two cases of polar lows, one in the Iceland and Greenland Seas and the other in the Labrador Sea. In particular, we focus on the effects of PLs on air-sea fluxes near the sea ice margin and from polynyas and leads, as well as on water mass transformation and mixed layer depth.

PLs form over the open ocean along the sea ice edge or boundary layer fronts (Rasmussen & Turner, 2003), which are narrow areas of strong temperature gradients or shear and convergence lines. They often develop in association with marine cold air outbreaks (CAOs, Papritz & Spengler, 2017), in which cold and dry polar air is advected over the relatively warm ocean, causing large heat fluxes from the ocean to the atmosphere near the sea ice edge. When a PLs forms near the sea ice edge, it can itself trigger a CAO, which amplifies heat loss from the ocean. About 60 to 80 % of the wintertime heat loss of the subpolar North Atlantic is caused by intermittent CAOs (Smedsrud et al., 2022), about two-thirds of which are accompanied by polar mesoscale cyclogenesis (Terpstra et al., 2021).

The direct effect of CAOs on the ocean mixed layer and dense water formation have been recently observed in the Iceland Sea (Harden et al., 2015; Renfrew et al., 2023) and in the Greenland Sea (Svingen et al., 2023). The more frequent and more intense the CAOs are during a winter, the deeper the mixed layer becomes. During CAOs in the Iceland Sea, surface heat fluxes of more than $200\,\mathrm{W\,m^{-2}}$ were observed from buoys that typically occur every 1-2 weeks in winter, lasting for 2.5 days on average (Harden et al., 2015). The Iceland and Greenland Seas are both important areas for the formation of dense water (Våge et al., 2022; Brakstad et al., 2023) contributing to the Denmark Strait Overflow Water (DSOW) with a delimiting density of $27.8\,\mathrm{kg\,m^{-3}}$ (Dickson & Brown, 1994), which leaves the Nordic Seas and becomes part of the deep return branch of the Atlantic Meridional Overturning Circulation (AMOC, Buckley & Marshall, 2016; Renfrew et al., 2019). From recent observations, it appears that dense water formation east of Greenland is of particular importance to the strength and variability of the AMOC (Lozier et al., 2019), particularly in the Nordic Seas (Chafik & Rossby, 2019).

However, PLs have been studied almost exclusively with regional atmospheric models (Jung et al., 2016), with recent representations also in global atmosphere models (Bresson et al., 2022). To our knowledge, only two studies have been conducted with coupled models. A three-day long simulation with a regional model for the Barents Sea with a resolution of 5 km (Wu, 2021) and one with a global model Hallerstig et al. (2021), with varying resolution in the atmosphere (18 to 5 km) and a 0.25 ° ocean. A high horizontal resolution of the atmospheric model leads to a better representation of wind speed (Kolstad, 2015; Mc Innes et al., 2011), surface heat fluxes, and atmospheric water cycle (Spensberger & Spengler, 2021) during CAOs, but also of mesoscale wind systems around Greenland (Gutjahr & Heinemann, 2018), such as tip jets (Doyle & Shapiro, 1999; Pickart et al., 2003), katabatic storms, and PLs (Klein & Heinemann, 2002; Kristjánsson et al., 2011; Gutjahr et al., 2022). It has also been recognized that a coupling to a dynamical sea ice and ocean model is necessary to improve the simulation of PLs (Jung et al., 2016). A kilometer-scale resolution ($\leq 5\,\mathrm{km}$) in the ocean model improves the representation of small-scale processes, such as ocean eddies, or leads and polynyas in the sea ice (Wang et al., 2016). Polynyas are recurrent areas of open water in an otherwise closed sea ice cover that tend to occur in the same location (Morales Maqueda et al., 2004), whereas leads are transient kinematic features that can occur everywhere in the ice.

In addition to formation of dense water in the open ocean, it also forms on Arctic continental shelves within coastal polynyas where heat is lost and compensated for by the formation of sea ice, releasing brine into the ocean beneath the ice (Cornish et al., 2022). These brine-enriched shelf waters descend down the slopes into deeper layers. If the resolution of the ocean model is too coarse, polynyas are not be represented, leading to biases in the properties of the deep water in the Arctic Mediterranean (Heuzé et al., 2023). The fracturing of sea ice has been observed during the passage of synoptic-scale cyclones, increasing the air-sea fluxes, but also enhancing lateral melting (Graham et al., 2019). However, whether PLs affect the sea ice and polynyas due to their much shorter timescale is less clear.

The question, then, is how the ocean and sea ice respond to resolving PLs in a fully coupled climate model of kilometer-scale. Global climate models have reached the kilometer scale (Hohenegger et al., 2023) and are capable of resolving all necessary processes, including mesoscale wind systems and PLs, boundary layer fronts, and deep convection in the atmosphere, mesoscale eddies in the ocean, and leads and polynyas in sea ice. In the ocean, unresolved (sub)mesoscale processes are thought to be important for the large-scale response of the climate system (Hewitt et al., 2022) and the role of small-scale ocean processes on large-scale climate needs to be investigated. In this study, we make a first step in this direction by explicitly resolving PLs, ocean eddies, polynyas and leads in a globally coupled simulation of kilometer-scale. We investigate the effects of PLs on the ocean and sea ice using the globally coupled ICON (Icosahedral Nonhydrostatic)-Sapphire

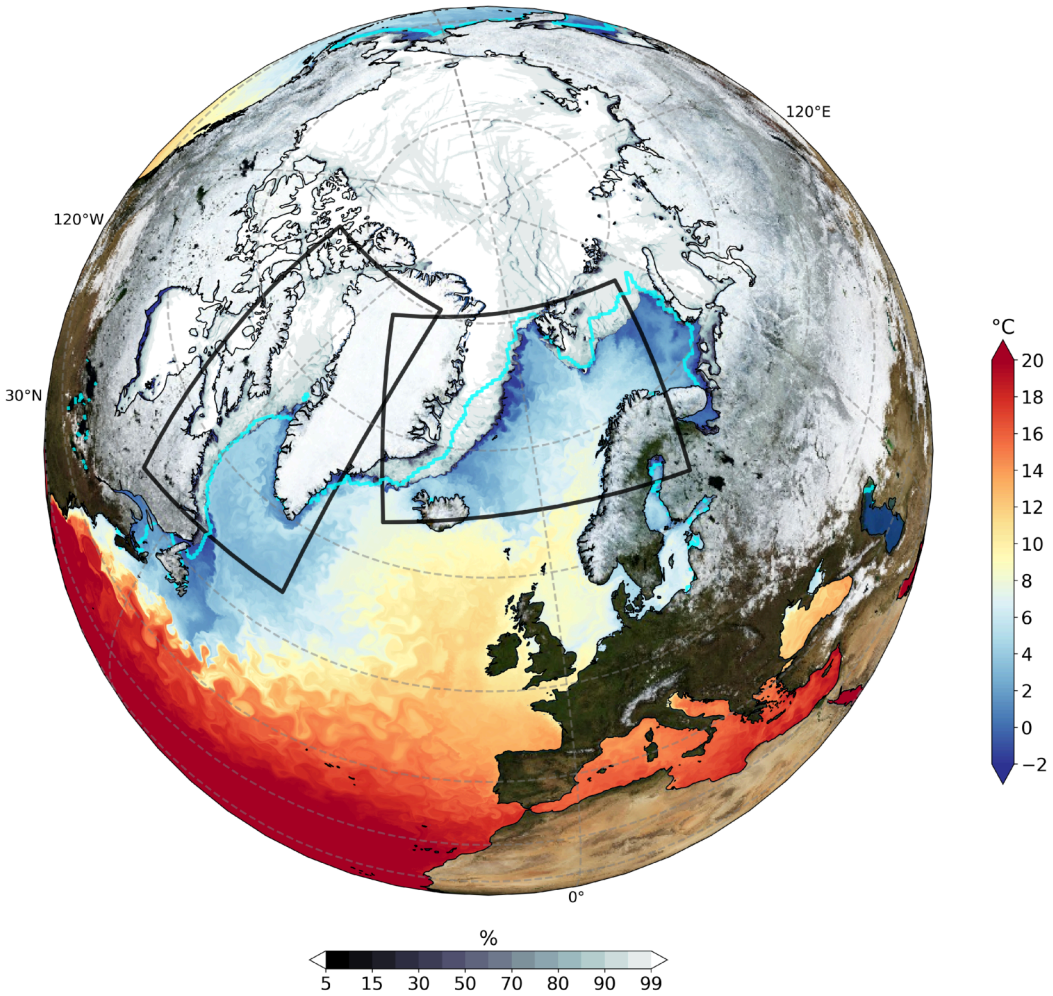

Figure 1. Global sea surface temperature and sea ice concentration simulated by the coupled ICON2.5 (2.5 km horizontal resolution) for 3 February 2020 at 0 UTC. Overlaid is daily mean 15 % ice concentration (cyan) from EUMETSAT OSI SAF v3.0 (OSI-450a, Lavergne et al., 2019) for the same day with a resolution of 25 km. (NASA's true color blue marble image from Terra at 0.1°over land (`https://neo.gsfc.nasa.gov/view.php?datasetId=BlueMarbleNG-TB`). The black boxes mark the two case study areas for the Iceland/Greenland and Labrador Seas.

model at a horizontal resolution of 2.5 km in the atmosphere, ocean, sea ice and land. Because the simulation is relatively short (72 days), we focus on two case studies of PLs, one over the Iceland and Greenland Seas and one over the Labrador Sea, in which we demonstrate the effect of PLs on the upper ocean and sea ice. The case studies discussed do not have real-time counterparts because the coupled model ran freely after its initialization on 20 January 2020. Therefore, all time and date information in the following refers to the relative time in the simulation.

The remainder of the manuscript is organized as follows. In section 2, the ICON-Sapphire model and its configuration is described. In section 3 and section 4, we present the results for the case studies in the Iceland and Greenland Seas and the Labrador Sea, respectively. In section 5 we summarize the results and draw conclusions.

Table 1. Overview of the globally coupled ICON-Sapphire 2.5 km simulation.

Parameter	ICON2.5
horizontal resolution	r2b10 (2.5 km)
# vertical levels (atm/oce)	90/112
Δ z-levels (oce)	6 to 532 m
Δt (atm/oce)	20 s/80 s
coupling frequency	12 min
simulation period	2020-01-20 to 2020-03-31 (72 d)
output volume	∼ 340 TB (135 TB/month)
output frequency	2d-atm. (30 min), 3d-atm. (1 d),
	2d-oce (1 h, 3 h), 3d-oce <200 m (3 h), 3d-oce (1 d)

2 ICON-Sapphire model configuration

We use a globally coupled simulation (ICON2.5) created with ICON-Sapphire (G_AO_2.5km in Hohenegger et al., 2023). ICON-Sapphire is a storm- and eddy-resolving version of ICON-ESM (Jungclaus et al., 2022) under the nextGEMS project (`https://nextgems-h2020.eu/`), which is a successor to DYAMOND Winter (Stevens et al., 2019). The objective of ICON-Sapphire is to use as few parameterizations as possible, retaining only those necessary to represent physical processes that cannot be represented at kilometer scales. ICON2.5 was run at a horizontal resolution of 2.5 km (Fig. 1 and Tab. 1) in both the atmosphere and land (ICON-A, Giorgetta et al., 2018)) and ocean/sea ice components (ICON-O Korn, 2017; Korn et al., 2022) for three months (72 days), beginning on 20 January 2020 and ending on 31 March 2020. This high global resolution resolves PLs in the Arctic Mediterranean, such as the Iceland, Greenland and Labrador Seas, kinematic features in sea ice, and a large part of the mesoscale ocean eddies in the Nordic Seas. We briefly describe the main features of this configuration, a more complete overview can be found in Hohenegger et al. (2023).

2.1 Atmosphere and land

The atmosphere was initialized from the European Centre for Medium-Range Weather Forecasts (ECMWF) operational analysis for 20 January 2020. ICON-A uses 90 vertical levels, with the top height at 75 km and layer thicknesses ranging from 25 to 400 m. In ICON-A only a minimum set of parameterizations is used, namely for radiation, microphysics, and turbulence. In ICON-A, radiation is parameterized by the Radiative Transfer for Energetics RRTM for General circulation model applications Parallel (RTE-RRTMGP) scheme (Pincus et al., 2019). Microphysics are parameterized with a one-moment scheme (Baldauf et al., 2011), which predicts the specific mass of water vapour, cloud water, rain, cloud ice, snow and graupel. Although all hydrometeors are advected by the dynamics, only cloud water and ice are mixed by the turbulence scheme and are optically active. No parameterization is used for subgrid-scale clouds, so grid boxes are either binary covered by clouds or cloud-free. Turbulence is parameterized with the Smagorinsky scheme (Smagorinsky, 1963) with modifications by Lilly (1962). Surface fluxes are computed according to Louis (1979). Land processes are simulated by the JSBACH land surface model (Reick et al., 2021).

2.2 Ocean and sea ice

The ocean was spun up from a complex simulation (see Hohenegger et al. (2023) for details) forced with climatological, NCEP, and ERA5 reanalyses using the Polar Sci-

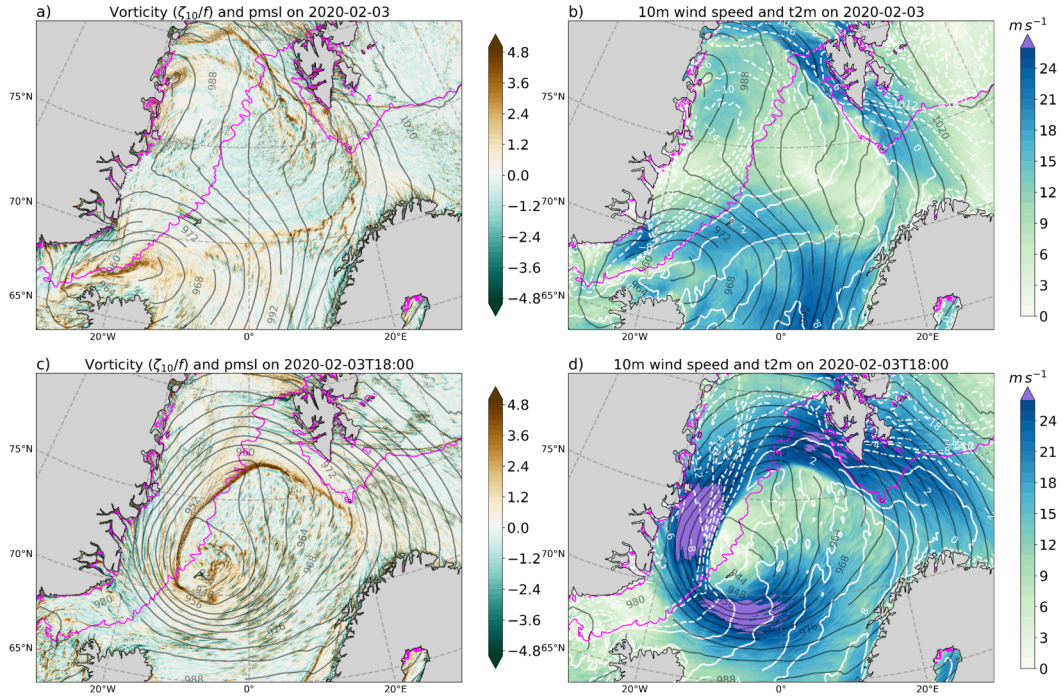

Figure 2. ICON2.5 snapshot (30 min mean) of (a,c) atmospheric relative vorticity (ζ) at 10 m height scaled by planetary vorticity (f) and (b,d) 10 m wind speed for 2020-02-03 0 UTC and 2020-02-03 18 UTC. Overlaid in all figures is the mean sea-level pressure (pmsl every 4 hPa; solid dark grey contours) and additionally in (c,d) the 2 m temperature in white (dashed for negative, solid for positive).

ence Center Hydrographic Climatology (PHC) version 3.0 observational data set (Steele et al., 2001) as initial conditions. ICON-O uses 112 vertical z-levels with a free ocean surface. The thickness of the ocean layers range from 6 to 532 m. Similar to the atmosphere, only a minimal set of parameterizations is used in ICON-O. Velocity dissipation (or friction) is parameterized by a "harmonic" Laplace operator. Turbulent vertical mixing is parameterized based on the turbulent kinetic energy (TKE) equation (Gaspar et al., 1990), in which a mixing length approach for the vertical mixing coefficient for velocity and oceanic tracers is used (Blanke & Delecluse, 1993).

In the current ICON-O version, sea ice thermodynamics are described by a single-category, zero-layer formulation (Semtner, 1976). Sea ice dynamics is based on the dynamics component of the Finite-Element Sea Ice Model (FESIM) (Danilov et al., 2015), see Korn et al. (2022). The sea ice model solves the momentum equation for sea ice with an elastic-viscoplastic (EVP) rheology (Hunke & Dukowicz, 1997).

Sea ice growth was not stored as an output variable, so we calculated potential ice production in polynyas from model output (Gutjahr et al., 2016; Zhou et al., 2023):

$$\rho_i L_i \frac{\partial h}{\partial t} = F_c - F_o, \tag{1}$$

with the constant sea ice density $\rho_i = 916.7\,\mathrm{kg\,m^{-3}}$, $L_i = 0.3337 \cdot 10^6\,\mathrm{J\,kg^{-1}}$ the latent heat of fusion for ice, and F_o the ocean heat flux (positive ablates the ice). The conductive heat flux through the ice (F_c) is assumed to be balanced by the net surface heat flux Q:

$$F_c = F_{sw} + F_{lw} + F_{sh} + F_{lh} = Q, \tag{2}$$

with F_{sw} and F_{lw} the net shortwave and long wave radiation fluxes, and F_{sh} and F_{lh} the turbulent sensible and latent heat fluxes.

Ice growth $\frac{\partial h}{\partial t}$ (in $\mathrm{m\,s^{-1}}$) is computed per grid cell as

$$\frac{\partial h}{\partial t} = \frac{Q - F_o}{\rho_i L_i}. \tag{3}$$

New ice growths if the ocean is losing heat ($Q - F_o > 0$). This approach assumes that the seawater is at the freezing temperature and that newly formed ice is immediately transported away, leaving the polynya open.

We then compute the daily ice volume growth within a polynya (all open water), as follows (Cheng et al., 2017; Zhou et al., 2023):

$$V = tA(1 - SIC)\frac{\partial h}{\partial t}, \tag{4}$$

with t=86400 s (1 day) and A the area of the grid cell, SIC the sea ice concentration and hence $A(1-SIC)$ the area of open water within a grid cell. The total daily ice production (in $\mathrm{m^3}$) is than summed up within the black box shown in Fig. 6.

2.3 Data output frequency and preprocessing

The 2d surface fields are available as 30-minute averages for the atmosphere and as 1-hour means for the ocean. 3d atmospheric fields are available as daily means and for the ocean the total depth levels are available as daily means and the upper 200 m as 3-hourly means. We have interpolated all ICON2.5 fields onto a regular 2.5 km grid by a nearest-neighbour method.

3 Polar low in the Iceland and Greenland Seas

The first case study describes the formation of a PL at the sea ice edge in the Iceland Sea. The polar low developed from a mesoscale lee cyclone from the Irminger Sea,

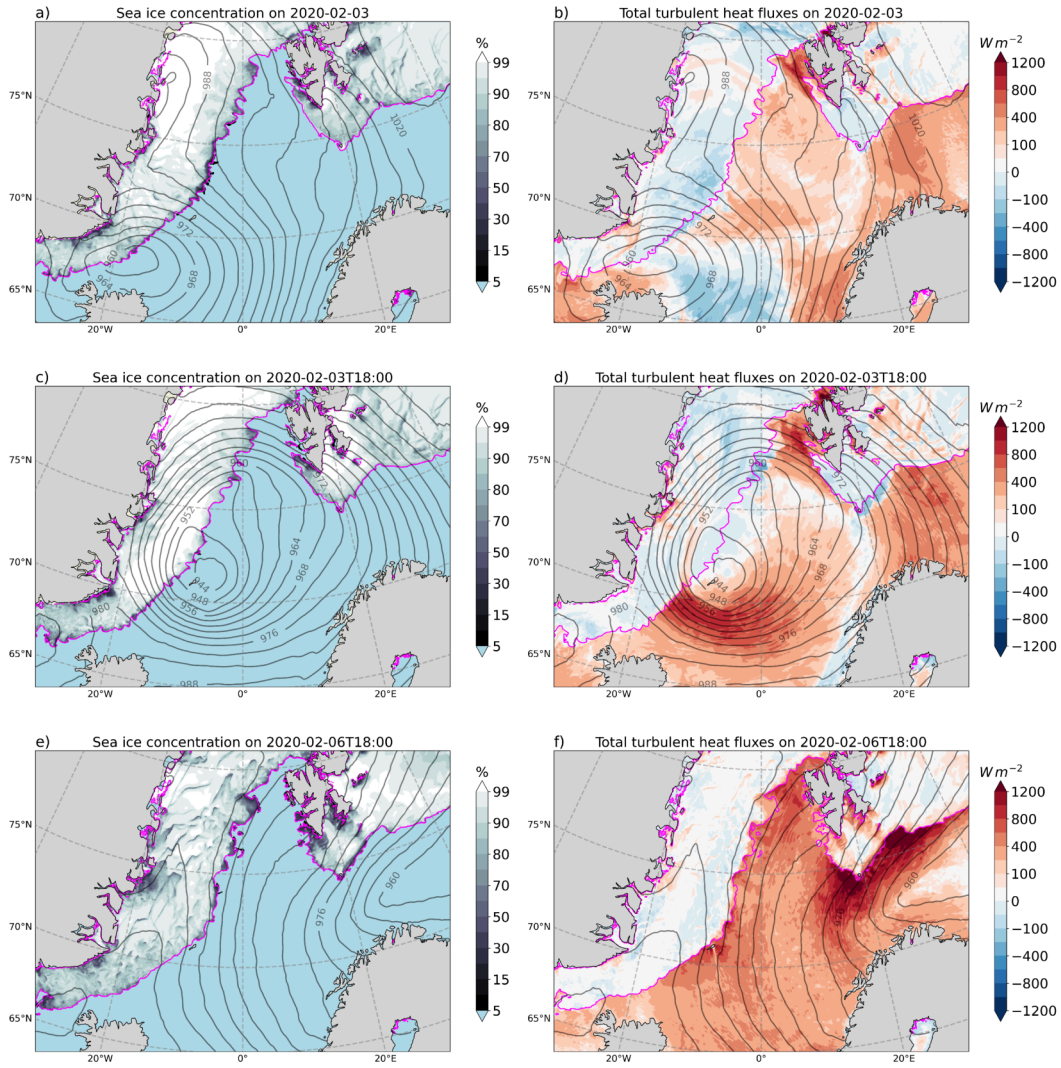

Figure 3. Evolution of the polar low from 2020-02-03 to 2020-02-06 in ICON2.5: (a,c,e) Sea ice concentration (color shaded) and (b,d,f) total turbulent heat fluxes (latent+sensible, colour shaded). The grey contours in all figures is the mean-sea level pressure (pmsl, every 4 hPa). Positive values means a heat flux from the ocean into the atmosphere.

which acted as a precursor (not shown). The PL migrates along the sea ice edge before crossing the Greenland and Norwegian Seas and reaching the Barents Sea three days later (section 3.1). During its passage, strong northerly winds cause a CAO from the sea ice of the EGC, resulting in a strong heat loss from the Iceland and Greenland Seas, forming sufficiently dense water to contribute to the DSOW (section 3.2). Over the northeast Greenland shelf, the strong northerly winds open leads in the sea ice and polynyas along the coast, such as the Sirius Water Polynya (SWP) (section 3.3). Compared to OSI SAF v3 (Lavergne et al., 2019), the sea ice concentration in ICON2.5 reaches too far east in the Iceland and Greenland Seas (see Fig- 1), which will have an effect on the location of dense water formation, as we will explain below.

3.1 Polar low formation

On 2 February 2020 a mesoscale lee cyclone formed over the Irminger Sea and crossed Iceland. Descending southerly winds from Iceland and their diabatic warming and vorticity stretching led to an increase in positive (cyclonic) relative vorticity north of Iceland. Furthermore, warm air advection northeast of Iceland contributed to additional cyclonic vorticity generation. Due to these processes, the boundary layer front at the sea ice edge north of Iceland became unstable (visible as a strong shear line with positive vorticity of $\zeta/f > 3.0$ in Fig. 2a).

At the same time, an upper-level shortwave trough with a length scale of about $L = 400\,\mathrm{km}$ was present over the Iceland Sea and associated with a positive vorticity anomaly (PVA). Weak stratification below 500 hPa with a mean Brunt-Väisälä frequency of about $N = 8{\cdot}10^{-3}\,\mathrm{s}^{-1}$ at the sea ice edge and a planetary vorticity at 66.9° N of $f = 1.34\,\mathrm{s}^{-1}$ results in a Rossby penetration depth of about $H = fL/N = 6.7\,\mathrm{km}$. Therefore, the cyclonic circulation associated with the upper-level PVA can easily reach the sea surface and amplify the lower-level PVA at the sea ice edge (Rasmussen & Turner, 2003).

As a result, the cyclone deepens rapidly, and the core pressure drops accordingly to about 960 hPa at 0 UTC on 3 February 2020 (Fig. 2a,b). 18 hours later, the core pressure drops further to 942 hPa (Fig. 2c,d) as the upper-level PVA and polar low move northeastward along the sea ice edge. The PL has sharply defined fronts (Fig. 2c) and its size is of meso-α scale (Orlanski, 1975) but it resembles cases described by Rasmussen and Turner (2003). The 10 m wind speed reaches hurricane force ($U_{max} = 34\,\mathrm{m\,s}^{-1}$) over the sea ice at 18 UTC on 3 February 2020 (Fig. 2d) and values of more than $28\,\mathrm{m\,s}^{-1}$ over the Iceland and Greenland Seas. The strong off-ice wind advects cold and dry polar air over the relatively warm Iceland and Greenland Seas in a CAO.

3.2 Heat loss from the ocean and Denmark Strait Overflow Water formation in response to a polar low

Figure 3 shows the evolution of the PL from 3 to 6 February 2020. After its formation at the sea ice edge, the low travels along the ice edge before it crosses the open ocean south of Svalbard into the Barents Sea. The strong northerly winds over the sea ice of the EGC cause the ice to break forming leads, which is especially visible on 6 February 2020 (Fig. 3e). Near the northeast coast of Greenland also polynyas open up, such as the Scoresby Sund and the Sirius Water polynyas (see section 3.3), or the Storfjorden Polynya in southern Svalbard.

The strong winds of the PL and the CAO lead to strong turbulent heat fluxes near the ice edge in the Iceland Sea, but also over the Greenland Sea as the PL moves northward along the ice edge. During its mature state at 18 UTC on 3 February 2020, the total turbulent (latent + sensible) heat flux (THF) reaches values of more than $1500\,\mathrm{W\,m}^{-2}$ over the Iceland Sea (Fig. 3d). Over the Scoresby and Sirius Water polynyas the THF is about $400\,\mathrm{W\,m}^{-2}$. Strong wind speeds lead further to a THF of more than $1000\,\mathrm{W\,m}^{-2}$

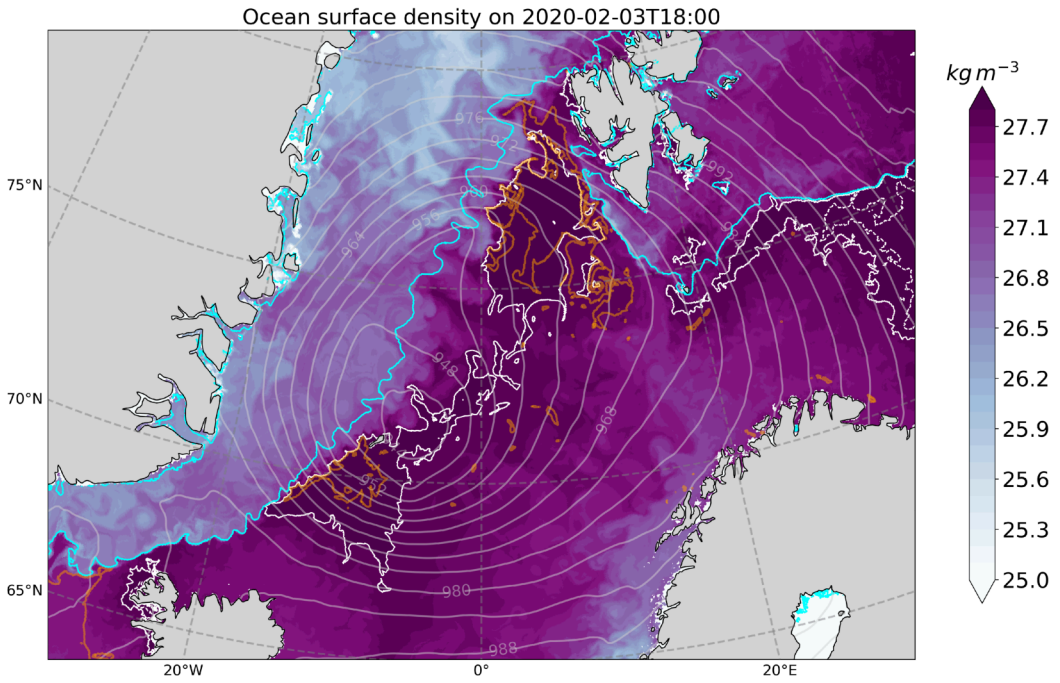

Figure 4. Potential density (σ_θ) at the ocean surface on 2020-02-03 at 18 UTC in ICON2.5. Overlaid as contours is mean-sea level pressure (light grey, every 4 hPa), the 15 % sea ice concentration (cyan), the outcropping 27.8 kg m^{-3} (solid white) and 27.9 kg m^{-3} (dashed white) isopycnals, and the mixed layer depth exceeding 400 m (orange).

over Fram Strait and the Storfjorden Polynya, which is the primary source for brine-enriched shelf waters(e.g. Skogseth et al., 2004, 2008). When the PL reaches the Barents Sea, it causes THF values of more than 1500 W m^{-2} due to a CAO from the sea ice over the relatively warm ocean surface of the Barents Sea.

Over the Iceland and Greenland Seas, the strong heat fluxes pose a strong buoyancy loss of the upper ocean and hence a potential source for dense water formation. Figure 4 shows the potential density (σ_θ) at the ocean surface at 18 UTC on 3 February 2020. Directly along the sea ice in the Iceland and Greenland Seas, dense water ($\geq$ 27.8 kg m^{-3}) outcrops at the surface. A density of 27.8 kg m^{-3} is the delimiter for overflow water (Dickson & Brown, 1994). Water denser than this threshold contributes to the DSOW, the densest water mass that is able to leave the Nordic Seas through Denmark Strait, where it contributes to the Deep Western Boundary Current. North of Jan Mayen, the outcrop of the 27.8 kg m^{-3} isopycnal is interrupted by buoyant eddies resulting from baroclinic instabilities of the EGC (Foukal et al., 2020) that become part of the reflecting Jan Mayen Current (Bourke et al., 1992). The eddies transport cold and fresh polar surface water into the Greenland Sea Gyre, suppressing the formation of dense water. The cold SST of these eddies can be seen from Fig. 1. The mixed layer reaches depths of more than 400 m in the Iceland Sea south of Jan Mayen and in Fram Strait.

To quantify the effect of the PL on the DSOW formation, we computed the water mass transformation (WMT), $F(\sigma_\theta)$ in units of m^3 s^{-1}, for the density class (or bin size) enclosed by the outcropping isopycnal of $\sigma_\theta = 27.85 \pm 0.05$ kg m^{-3}, following the approach of Petit et al. (2020) and Speer and Tziperman (1992). We first compute the buoyancy flux (B) at the ocean surface from 6-hourly mean values, following Groeskamp et al. (2019) ($B > 0$ means a buoyancy loss of the sea surface water):

$$B = \overline{w'b'} = -\frac{\alpha}{c_p} Q_0 + \beta \frac{S}{1-S}(E-P), \tag{5}$$

with w' and b' fluctuations of the vertical velocity and buoyancy, $c_p = 4192.664\,\mathrm{J\,K^{-1}\,kg^{-1}}$ the specific heat capacity of sea water, Q_0 the net heat flux (in $\mathrm{W\,m^{-2}}$) at the ocean surface (positive into the ocean), α (in $\mathrm{K^{-1}}$) and β (in $\mathrm{psu^{-1}}$) the thermal expansion and haline contraction coefficients, S the salinity (in psu), P the precipitation (rain+snow+runoff) and E the evaporation (both in $\mathrm{m\,s^{-1}} \mathrel{\widehat{=}} \mathrm{kg\,m^{-2}\,s^{-2}}$). ICON-O uses the UNESCO equation of state (UNESCO, 1981) to compute α and β.

Then we calculate $F(\sigma_\theta)$ by integrating the buoyancy flux over the area A of the outcropping density class ($\sigma_\theta + \Delta\sigma_\theta/2$) with $\Delta\sigma_\theta = 0.1$:

$$F(\sigma_\theta) = \frac{1}{\Delta\sigma_\theta} \iint B\,\Pi\,(\sigma_\theta)\,dA, \tag{6}$$

where

$$\Pi(\sigma_\theta) = \begin{cases} 1, & \text{for } |\sigma_\theta - \sigma'_\theta| \leq \frac{\Delta\sigma_\theta}{2} \\ 0, & \text{otherwise} \end{cases} \tag{7}$$

is a filter that ensures that only the area A enclosed by a density class is integrated. We follow the convention that when $F(\sigma_\theta) > 0$, water is transformed towards a higher density.

Figure 5a shows the WMT to the density class of $\sigma_\theta = 27.85 \pm 0.05\,\mathrm{kg\,m^{-3}}$, which corresponds to DSOW, during the PL passage (3 to 6 February 2020). There is in particular DSOW forming in the Iceland Sea south of Jan Mayen, with local peak values of more than 8 mSv. The WMT is notably affected by the presence of mesoscale eddies in the ocean (as discussed for Fig. 4), which deforms the boundaries of the WMT area into elongated filaments. Over the entire simulation period of 72 days, the total WMT shows values of up to 80 mSv in a narrow band along the ice edge, extending from the Iceland Sea to Fram Strait. The relative WMT contribution from the PL (3 to 6 February 2020) onto the total WMT ranges from about 10 to 30 % (Fig. 5c), with highest values near the ice edge in the Iceland Sea and close to Jan Mayen.

Occasionally, buoyant eddies shedding from the shelf break EGC beneath the sea ice (Fig. 4) prevent dense water formation directly at the sea ice edge in our simulation, so that it is displaced further away from the sea ice in the Iceland and Greenland Seas. However, the sea ice in the Iceland Sea in our ICON2.5 simulation extends too far east compared to present-day conditions (see Fig. 1). Therefore, the WMT in our simulation erroneously occurs too far in the central Iceland Sea and not in its northwestern part (Våge et al., 2018; Spall et al., 2021; Våge et al., 2022) as observed in association with a retreating sea ice edge toward Greenland (Moore et al., 2022). Furthermore, we note that our simulation period is rather short and hence longer simulations of a similar resolution are required to quantify the effect of PLs on the climate scale.

A time series of the integrated WMT over the Iceland Sea (Figure 5d; averaged over the black box in Figure 5a-c) shows peak values of about 17 Sv, with one of the peaks coinciding with the studied PL from 3 to 6 February 2020. The time series also shows that there are episodes when DSOW formation is large, interspersed with intermittent periods of low or no formation. The largest formation rates in the simulation occur about a week after the studied PL, where there was an episode with high WMT for the density class $27.85 \pm 0.05\,\mathrm{kg\,m^{-3}}$, but even dense water ($27.95 \pm 0.05\,\mathrm{kg\,m^{-3}}$) formed in the Iceland Sea (Fig. A1). This strong WMT event is caused by a complex sequence of polar mesoscale cyclones in the period from 6 to 15 February that advect cold and dry polar air masses over the Iceland Sea in CAOs, which lead to persistent heat loss from the Iceland Sea. In contrast, the PL on 3 to 6 February advected polar air in a short-lived event over the Iceland Sea after which the wind direction turned to south and interrupted the CAO.

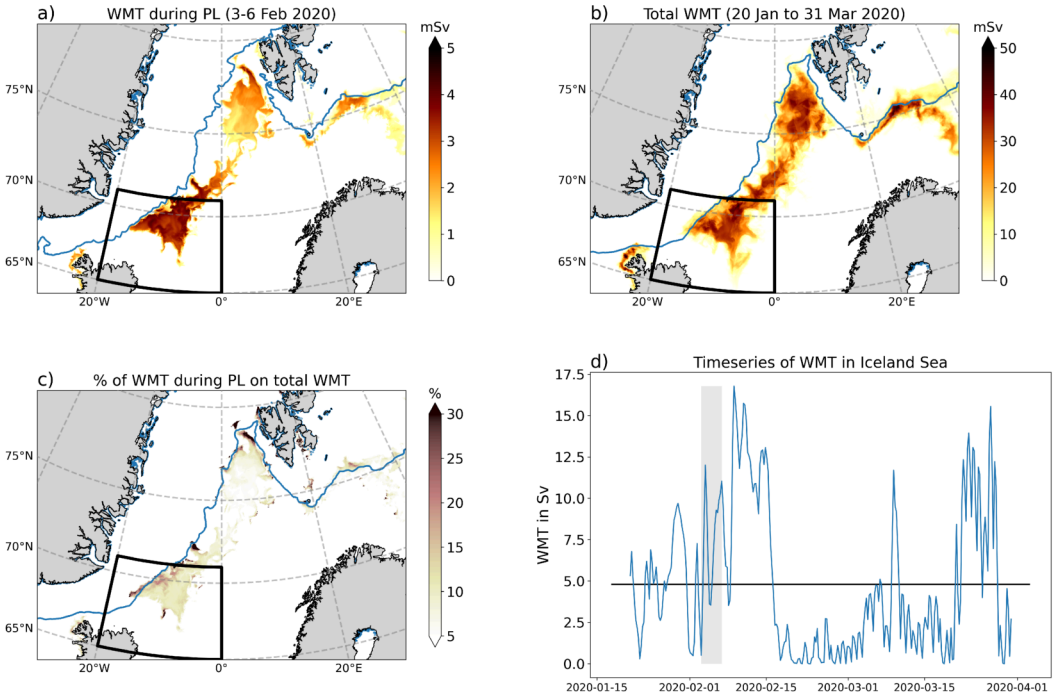

Figure 5. Water mass transformation (WMT), $F(\sigma_\theta)$, of the density class $\sigma_\theta = 27.85 \pm 0.05\,\mathrm{kg\,m^{-3}}$, which is the threshold density of the DSOW ($1\,\mathrm{mSv} = 10^{-3}\,\mathrm{Sv} = 10^{3}\,\mathrm{m^3\,s^{-1}}$). (a) WMT during the period of the polar low from 3 to 6 February 2020, (b) total WMT during the simulation period 20 January to 31 March 2020 (72 days), and (c) the relative contribution (%) of the polar low on the total WMT. The blue contour shows the 15 % sea ice concentration averaged over 3 to 6 February 2020 in a) and over 20 January 2020 to 31 March 2020 in b) and c). (d) Time series of integrated WMT in the Iceland Sea (black box in a-c). The grey shading marks the period of the polar low passage (3 to 6 February 2020). The horizontal line marks the temporal mean over the simulation (about 4.8 Sv).

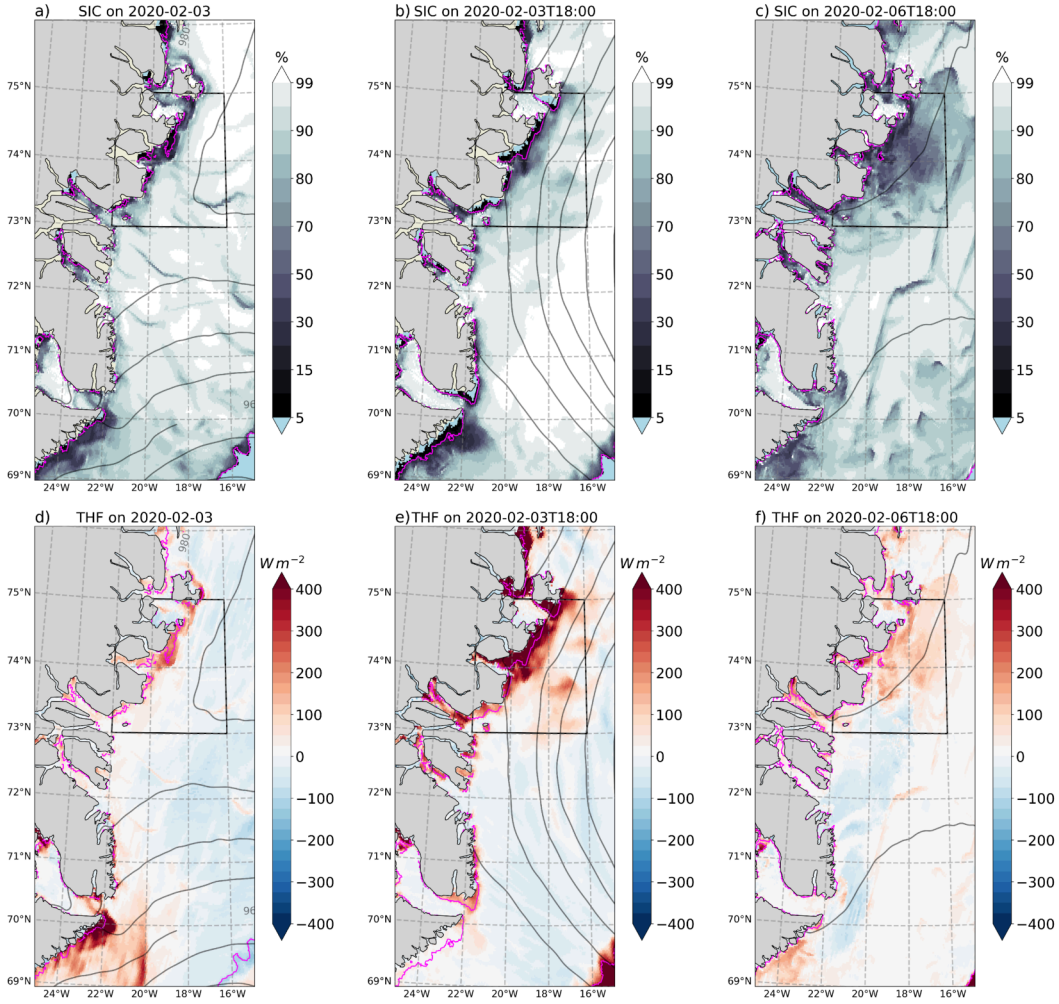

Figure 6. ICON2.5 snapshots of (a-c) sea ice concentration and (d-f) total turbulent heat flux (THF) at 18 UTC on 3 February 2020, and at 18 UTC on 6 February 2020, respectively. Positive values mean a heat loss from the ocean. Overlaid is the mean-sea level pressure (every 4 hPa). The black box marks the domain of the Sirius Water Polynya over which quantities were averaged to construct time series (Fig. 7).

The formation of DSOW is strongly depending ($r_s = 0.85, p < 0.01, n = 72$) on whether there is a CAO with a strong positive temperature gradient of the SST and the 2 m air temperature ($\Delta T = SST - T_{2m}$) and a wind blowing from the sea ice (Fig. A2). The correlation with both the latent ($r_s = 0.87, p < 0.01, n = 72$) and sensible heat flux is high ($r_s = 0.90, p < 0.01, n = 72$), but with wind speed alone rather weak ($r_s = 0.13, p = 0.03, n = 72$). The latter can be explained by the fact that a strong wind speed alone is not sufficient for WMT. The wind must come from the ice to lead to a simultaneously strong temperature contrast between the sea surface and the atmospheric boundary layer. The correlation coefficients were computed based on Spearman's ρ and the p values were computed based on a two-sided t test.

This result shows that PLs contribute to the formation of dense water exceeding the overflow water delimiter ($27.8\,\mathrm{kg\,m^{-3}}$) along the sea ice edge in the Iceland and Greenland Seas, renewing the climate-relevant DSOW.

3.3 Sirius Water Polynya - opening and heat fluxes during the polar low passage

The Sirius Water Polynya (SWP) is one of the most prominent polynyas of Northeast Greenland and located roughly between Shannon Ø and Pendulum Øer between 75°and 74° N (Pedersen et al., 2010). The polynya forms as an intermittent flaw polynya in the transition zone of the fast ice and the pack ice.

Figure 6 shows the sea ice concentration and THF along the northeast coast of Greenland during the passage of the PL. At 0 UTC on 3 February 2020 (Fig. 6a), only weak winds blow from the northeast in the area of the SWP, a remnant of a previous weaker polar low that moved over the sea ice along northeast Greenland, where it also produced sea ice leads and opened the SWP (visible in Fig 6a), resulting in a THF of about 200 to $300\,\mathrm{W\,m^{-2}}$ (Fig. 6d). East of Scoresby Sund, the wind direction is from the east during PL formation at the ice edge in Denmark Strait, which pushes the pack ice together, closing the leads but opening the Scoresby Sund Polynya along the Blosseville Coast (Fig. 6a,d).

At 18 UTC on 3 February 2020, the PL reaches mature state and moves northeastwards along the sea ice edge. On its backside, the wind turns to the northeast (Fig. 6b) and reaches values of more than $30\,\mathrm{m\,s^{-1}}$ in the area of the SWP (Fig. 2d). When the wind shifts to northerly directions and intensifies, the SWP opens (Fig. 6b), resulting in a strong heat loss from the ocean of more than $400\,\mathrm{W\,m^{-2}}$ (Fig. 6e). The location of the SWP is realistically simulated compared to a case study based on satellite data from Pedersen et al. (2010). Although the Scoresby Sund Polynya is still open, there are almost no THF because of the calm wind conditions. The northerly winds continue for the next three days until the PL reaches the Barents Sea. During this time, the SWP remains open and increases in size until it reaches its greatest extent on 6 February 2020 (Fig. 6c). Since the wind speed is very low on that day, the heat fluxes reach only values of about $200\,\mathrm{W\,m^{-2}}$. The persistent strong northerly winds have broken up the pack ice, and sea ice leads have formed (Fig. 6c), releasing heat with THF values of about 50 to $100\,\mathrm{W\,m^{-2}}$.

3.4 Time series of the Sirius Water Polynya and its control by polar lows in winter 2020

To quantify how polar lows affect the SWP over the entire simulation, we spatially averaged several quantities over the domain marked as a black box in Figure 6. Figure 7 shows the time series of daily means from 20 January to 31 March 2020. There is a clear connection of low ice concentration and large polynya area (Fig. 7a). We have marked all periods in which the SWP opened with Roman numbers (I to VII). The maximum polynya area is considerably larger in ICON2.5 with about $8{\cdot}10^3\,\mathrm{km^2}$ compared to about $1.4{\cdot}10^3\,\mathrm{km^2}$ reported by Pedersen et al. (2010) for February to May 2008. The larger

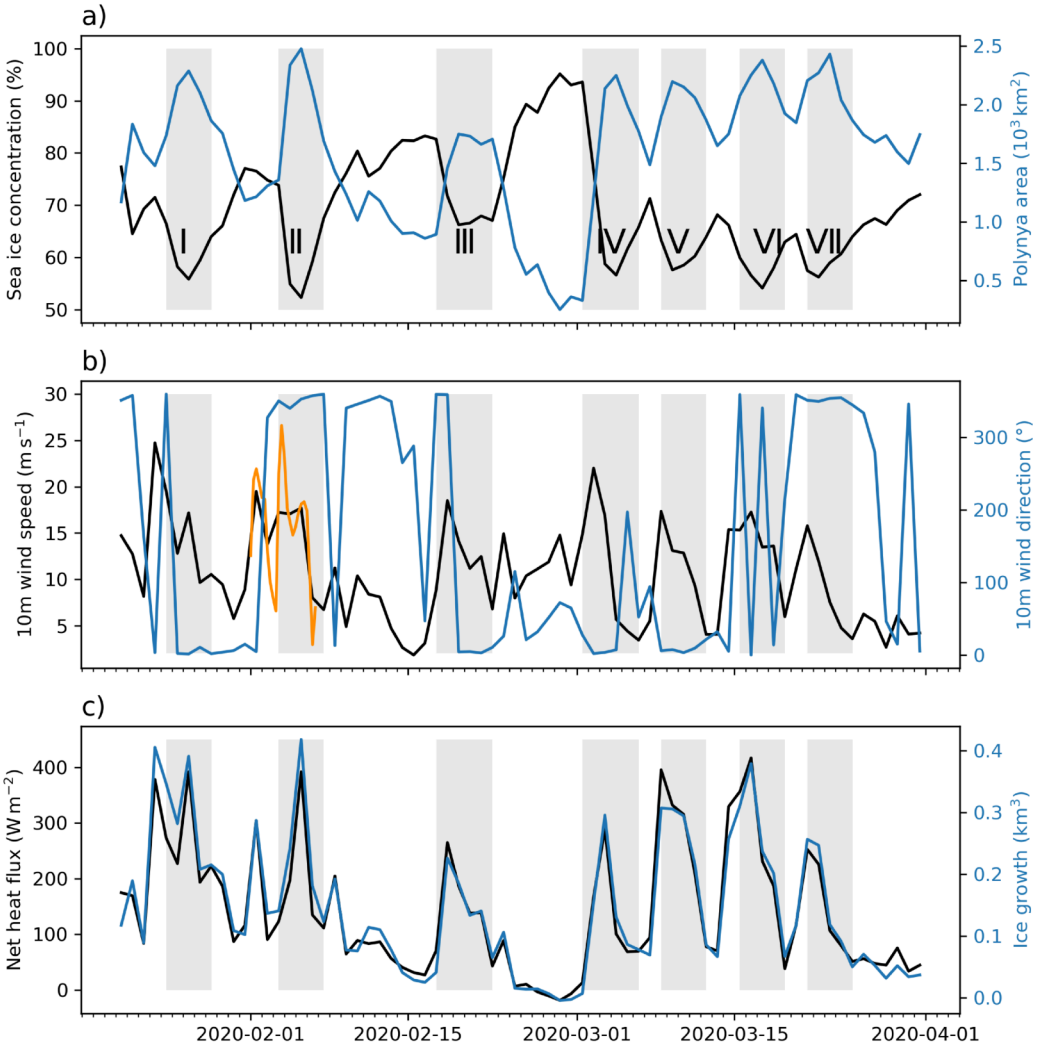

Figure 7. Time series of daily means of the entire ICON2.5 simulation period (20 January to 31 March 2020) of (a) sea ice concentration and polynya area (sum of open water area), (b) 10 m wind speed (30-minute values of the case study in orange) and direction, and (c) net heat flux and new ice formation. The Roman numbers (I-VII) and grey shading mark seven opening events of the Sirius Water Polynya in the ICON2.5 simulation.

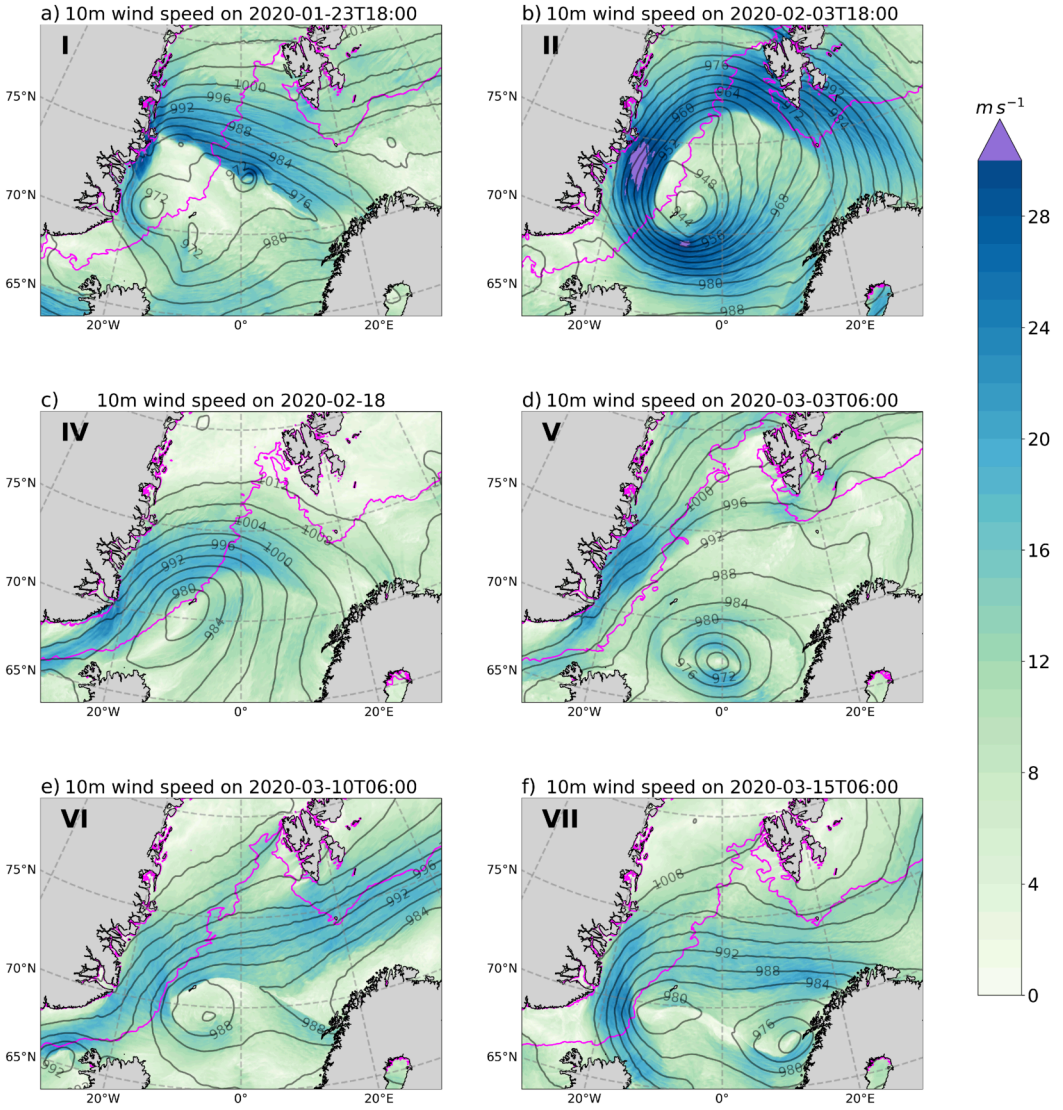

Figure 8. ICON2.5 snapshots of the 10 m wind field (color shaded) and mean-sea level pressure (contours; every 4 hPa) during opening events of the Sirius Water Polynya. The Roman numbers mark the event in the time series from Fig. 7a. Event number III has been left out because the polynya opening is rather weak compared to the other events.

polynya area may be due to several reasons, for instance Pedersen et al. (2010) used a threshold of 60 % sea ice concentration to define the polynya, or different environmental conditions prevailed in the winter of 2008 and 2020 determining sea ice conditions, or tuning of the sea ice rheology in our simulation.

At the beginning of each of these periods, the averaged daily wind speed shows a peak of about $20\,\mathrm{m\,s^{-1}}$ with a northerly to northeasterly direction (Fig. 7b) and a subsequent weakening. The polynya area and 10 m wind speed show the strongest correlation when the wind speed leads one day (lag1-correlation: $r_s = 0.42$, $p < 0.01$, $n = 72$). The correlation coefficient was computed based on Spearman's ρ and the p value was computed based a two-sided t test. This delayed response arises from the inertia of sea ice, but it is fast enough for the ice to respond to short-lived PLs. The wind peaks are even more visible in the 30-minute data (orange line in Fig. 7b). Each polynya opening is associated with a THF peak that leads to new ice formation (Fig. 7c), while ice formation outside of opening events is significantly reduced.

Each of these polynya opening events is associated with northerly winds of a polar low east of northeast Greenland (Fig. 8). All these PLs produce wind speeds above gale force in the area of the SWP. These results confirm that PLs are the primary cause of SWP opening and subsequent heat loss from the ocean, leading to new ice growth and associated brine rejection, resulting in the formation of brine-enriched shelf water over the Greenland continental shelf (not shown).

4 Polar low in the Labrador Sea

In the second case study, we analyse a PL that forms over the Labrador Sea during a CAO from Baffin Island that considerably intensifies when it encounters a boundary layer front at the sea ice edge (section 4.1). The PL is the strongest event in the simulation, causing a considerably heat loss from the open ocean that directly cools the boundary current and results in a deepening of the mixed layer. Along the coast of Labrador coastal polynyas form where additional heat is lost (section 4.2).

4.1 Formation of a hurricane-like polar low

Initially, a weaker precursor PL formed at the sea ice edge during a CAO and a shortwave trough at height, reaching the mature stage at 0 UTC on 20 February 2020 (this PL can be seen in Fig. 11a). This precursor PL intensified the CAO south of its core, so that strong winds blow parallel to the sea ice edge along the Labrador coast. These winds along the sea ice edge below a shortwave trough aloft destabilized the boundary layer front from which a baroclinic cyclone formed. This destabilizing mechanism by winds parallel to the sea ice edge is known to trigger polar lows (Heinemann, 1996; Drüe & Heinemann, 2001). The baroclinic cyclone was then steered north toward the sea ice and by reaching the sea ice edge at 12 UTC on 21 February 2020, it quickly intensified. The core pressure drops to 944 hPa and the winds intensify to hurricane force ($34\,\mathrm{m\,s^{-1}}$; Fig. 9a-b). Over the next 24 hours, the PL is steered to the south over the Labrador Sea before crossing into the Irminger Sea south of Cape Farewell, where it merges with a lee vortex.

The baroclinic intensification is driven by the strong temperature gradients across the boundary layer front along the sea ice that results in strong differential diabatic heating. This strong temperature contrast can be seen from the surface and 2 m temperature fields (Fig. 9c-d). The warm core of the PL is clearly visible from the 2 m temperature field. In addition, warm signatures from sea ice leads can be seen in the Baffin Bay and from coastal polynyas along the Labrador coast and around smaller island of Baffin Island, such as Resolution Island in front of the Meta Incognita Peninsula. This results shows how resolving leads and polynyas imprints warm anomalies on the atmospheric

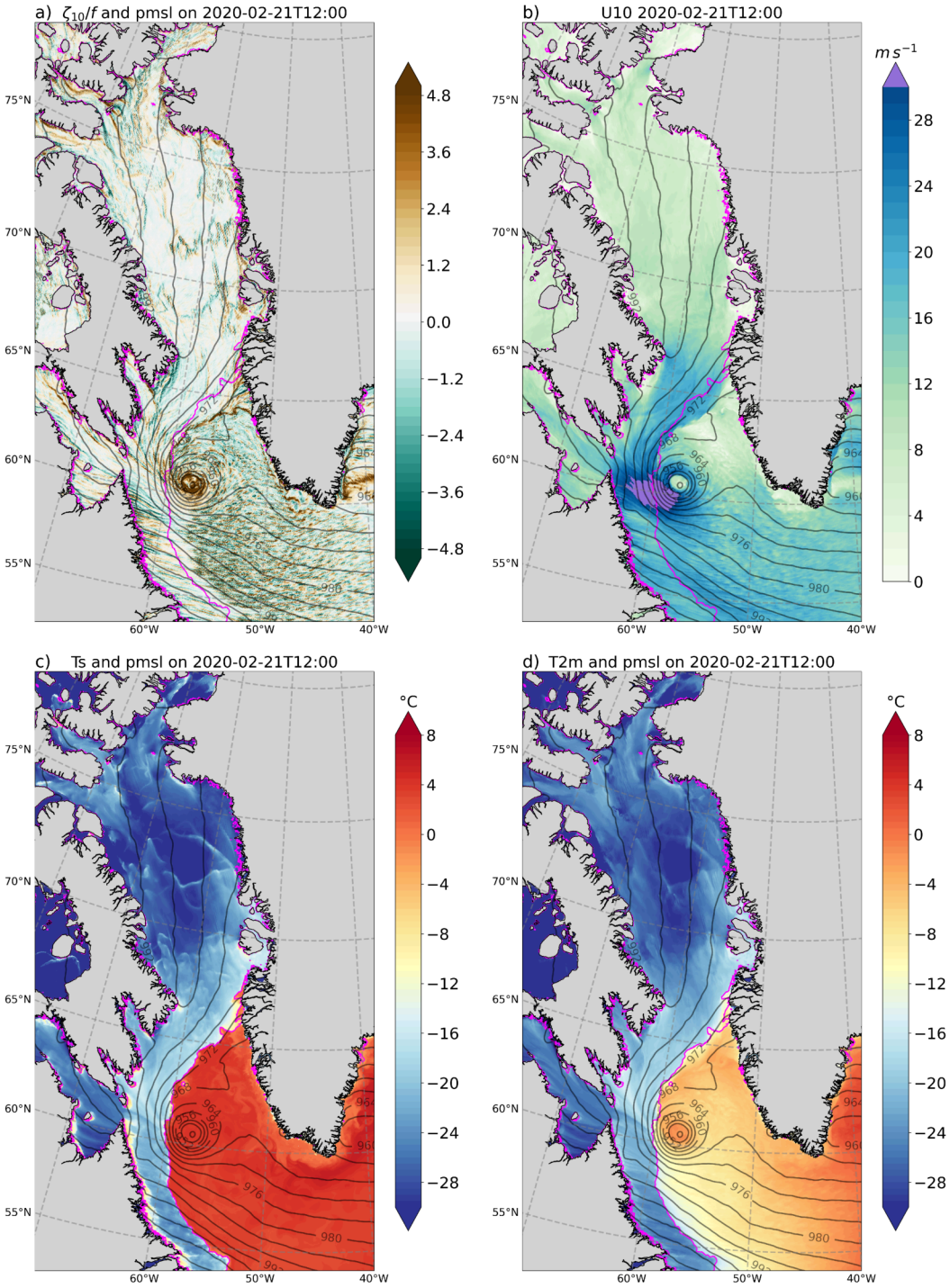

Figure 9. ICON2.5 snapshots of the Labrador Sea and Baffin Bay at 12 UTC on 21 February 2020 showing (a) scaled relative vorticity (ζ/f), (b) 10 m wind speed (U10; color shaded), (c) surface temperature (Ts), and (d) 2 m temperature (T2m). Overlaid is the mean-sea level pressure (pmsl) as grey contours (every 4 hPa) and the 15 % sea ice concentration (magenta).

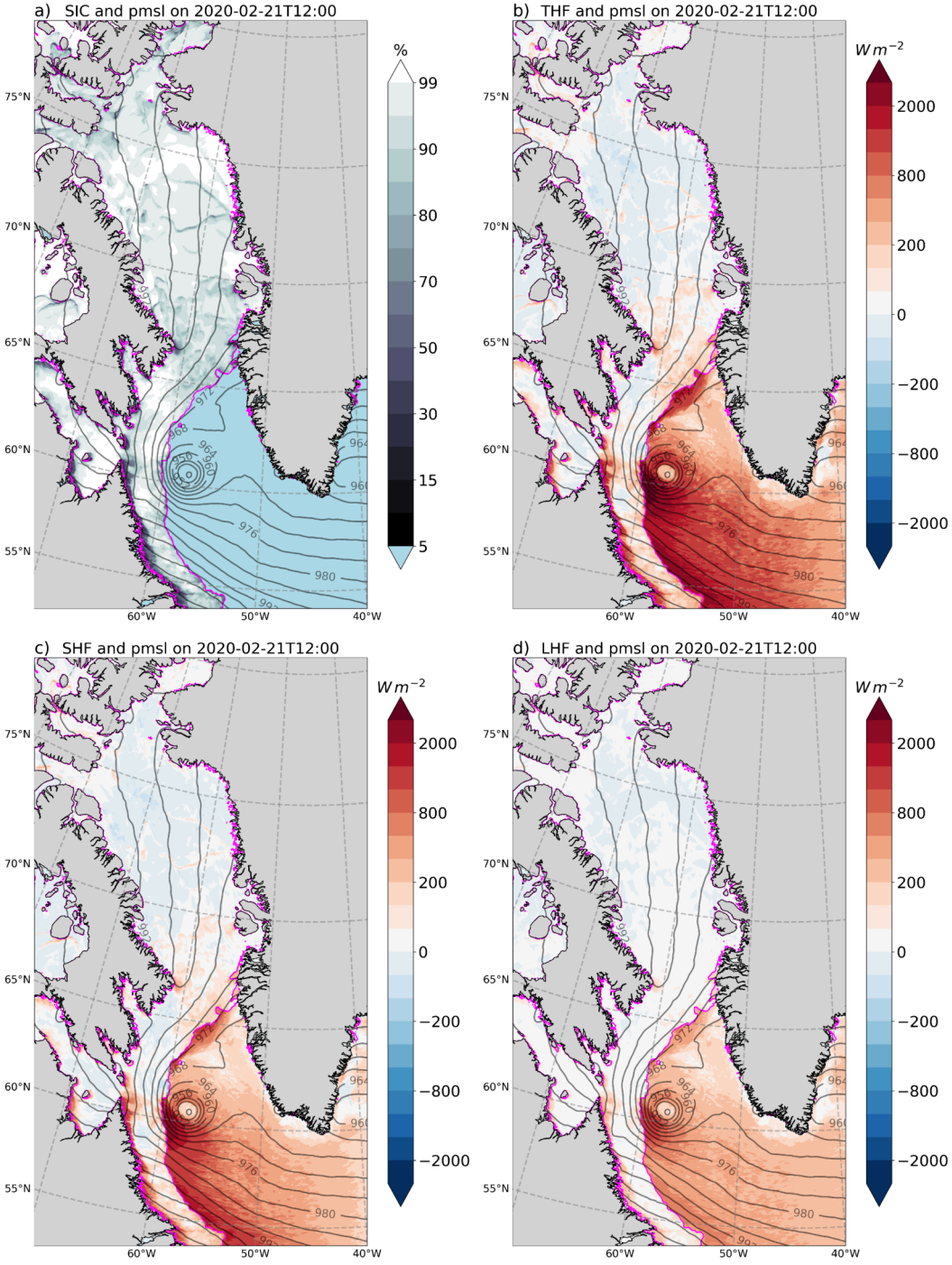

Figure 10. ICON2.5 snapshots of the Labrador Sea and Baffin Bay at 12 UTC on 21 February 2020 showing (a) sea ice concentration (SIC),(b) total turbulent heat flux (THF), (c) sensible heat flux (SHF), and (d) latent heat flux (LHF). Overlaid is the mean-sea level pressure (pmsl) as grey contours (every 4 hPa) and the 15 % sea ice concentration (magenta). Note the nonlinear colorbar in (b) to (d).

boundary layer over the sea ice, also by warm plumes that can extend several hundred kilometers downstream of polynyas (e.g. Gutjahr et al., 2016). The warmer near-surface temperatures could contribute to mediate the too cold atmospheric boundary layer over wintertime sea ice shown by CMIP6 models (Davy & Outten, 2020).

4.2 Heat fluxes and mixed layer deepening

Figure 10a shows the sea ice concentration at 12 UTC on 21 February 2020, where sea ice leads and polynyas can be clearly identified. The PL induces a strong CAO to the south of its core. The wind speeds of hurricane force induce THF values greater than $3000\,\mathrm{W\,m^{-2}}$ over the open water at the sea ice margin (Fig. 10b) that directly cool the boundary current. Large values of about $2000\,\mathrm{W\,m^{-2}}$ are also simulated further south over the Labrador Sea close to the sea ice. The sea ice breaks also south of the PL forming leads and polynyas where the ocean loses heat of about 200 to $1000\,\mathrm{W\,m^{-2}}$. Further north, THF values of $200\,\mathrm{W\,m^{-2}}$ are simulated over sea ice leads and less compact pack ice in the Baffin Bay in relation to strong northerly winds.

Splitting the THF into the sensible and latent heat flux (Fig. 10c-d) clearly shows that the sensible heat flux is larger close to the sea ice edge and in leads and polynyas. Although not the focus of this study, the strong heat fluxes near the PL core may cause the warm core as explained by the WISHE (Wind-induced surface heat exchange) mechanism. This mechanism intensifies the PL in a positive feedback, as was shown by (Wu, 2021) for the Barents Sea.

The strong heat fluxes cause a buoyancy loss of the upper-ocean that leads to a deepening of the mixed layer. Figure 11a shows the mixed layer depth (MLD) during the precursor PL at 0 UTC on 20 February 2020. Values of up to 800 m are simulated along the concave sea ice edge that decrease away from the sea ice. Buoyant mesoscale eddies shedding from the relatively warm Irminger Current (so called Irminger Rings) west of Greenland inhibit deep mixed layers in the northern part of the Labrador Sea.

About one day later (Fig. 11b), during the mature phase of the studied PL at 18 UTC on 21 February 2020, the MLD deepened by about 50 m over the open ocean (Fig. 11c). Higher values are reached directly at the sea ice edge. Another day later, after the PL has moved into the Irminger Sea, the MLD has deepened by about 100 m (Fig. 11d-e).

5 Summary and conclusions

For the first time, we present the simulation of polar lows (PLs) in a fully coupled global simulation (ICON-Sapphire) of kilometer-scale (2.5 km) in all of its components. The simulation resolves mesoscale cyclones, such as PLs in the polar region, and all relevant processes that are important for their formation, such as boundary layer fronts in the atmosphere, and for their effect on the ocean, such as mesoscale eddies or leads and polynyas in the sea ice.

Our results support that dense water forms in the Iceland and Greenland Seas near the marginal ice zone during cold air outbreaks (CAOs) induced by polar lows, which is in accordance to observations in the Iceland Sea (Våge et al., 2015; Renfrew et al., 2023) and in the Greenland Sea (Svingen et al., 2023). We demonstrate in two case studies that ICON2.5 is capable of simulating intense PLs over the Iceland, Greenland, and Labrador Seas. These PLs lead to significant heat loss from the ocean, as observed in other studies (e.g. Føre et al., 2012; Moreno-Ibáñez et al., 2021). The total turbulent heat flux (THF) easily reaches values greater than $1500\,\mathrm{W\,m^{-2}}$ at the sea ice margin, but the ocean also loses heat in sea ice leads and polynyas where the THF reaches values greater than $400\,\mathrm{W\,m^{-2}}$, which we illustrate for the Sirius Water Polynya (SWP) in northeast Greenland. The opening of the SWP is closely related to the presence of PLs east of Northeast Green-

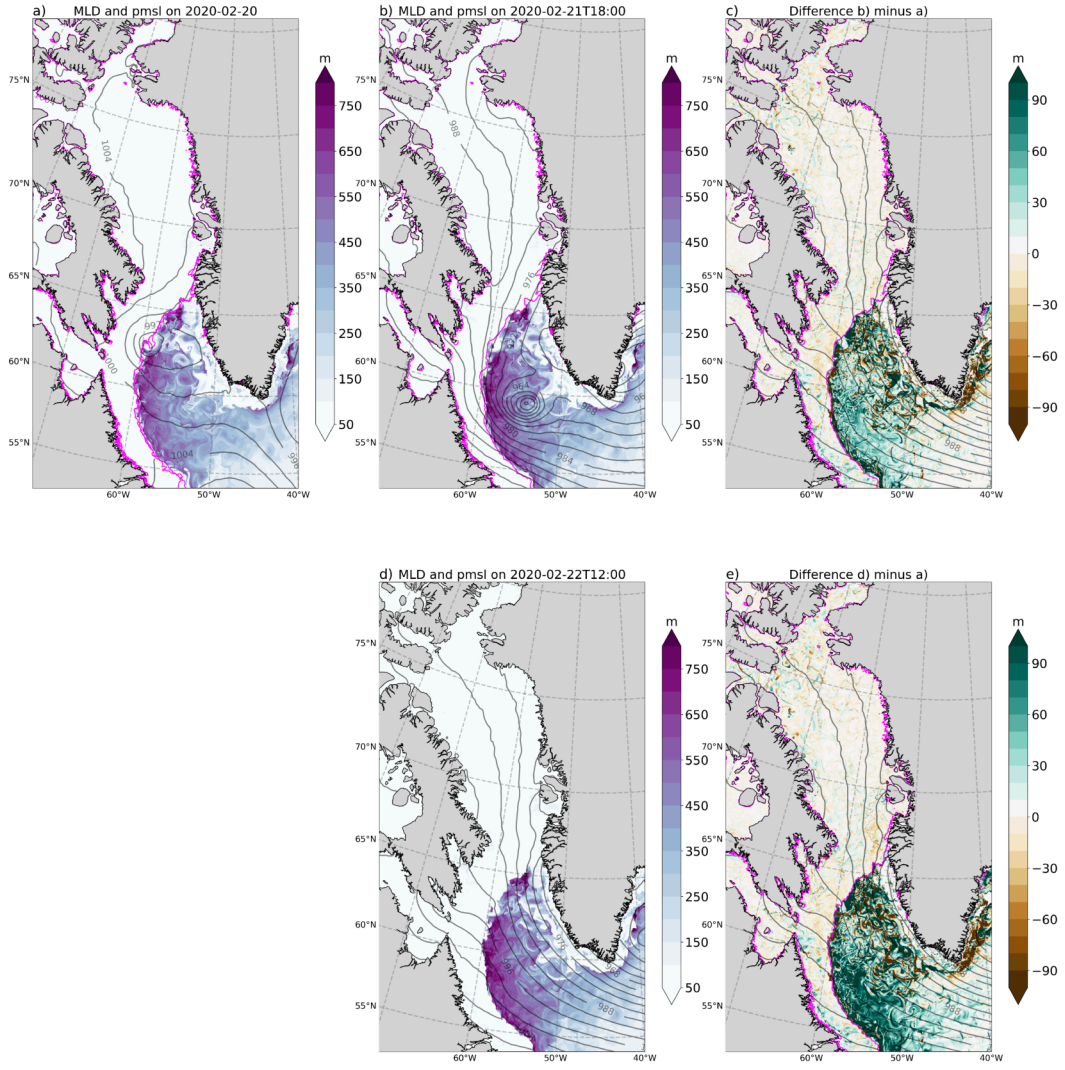

Figure 11. ICON2.5 snapshots of the Labrador Sea and Baffin Bay at 12 UTC on 21 February 2020 showing the mixed layer depth (MLD) on 20 February at (a) 0 UTC, (b) 18 UTC, and (c) the difference of (b) minus (a). The second row shows the MLD for (d) at 12 UTC on 22 February and (e) the difference (d) minus (a). Overlaid is the mean-sea level pressure as grey contours (every 4 hPa) and the 15 % sea ice concentration (magenta).

land, which induce strong northerly winds west of their centers, leading to divergent wind forcing of sea ice and the opening of the wind-driven SWP. During the opening events of the SWP, new ice forms, contributing to brine-enriched shelf water on the East Greenland shelf.

The most intense PL of hurricane force ($34\,\mathrm{m\,s^{-1}}$) was simulated over the Labrador Sea, where the enormous heat fluxes (THF of more than $3000\,\mathrm{W\,m^{-2}}$) occur. This strong buoyancy forcing leads to a mixing layer deepening of about 100 m within two days (or $50\,\mathrm{m\,d^{-1}}$), which is in the order of direct measurements with Langrangian floats (Steffen & D'Asaro, 2002) and larger than the $38\,\mathrm{m\,d^{-1}}$ observed with moorings in the Greenland Sea during strong CAOs (Svingen et al., 2023). The sensible heat flux was larger than the latent heat flux along the sea ice edge and within leads and coastal polynyas along the coasts of Labrador and Baffin Island. In addition, resolving leads and polynyas results in warm near-surface temperature anomalies that could influence the atmospheric boundary layer over the sea ice.

These results demonstrate the importance of resolving mesoscale polar lows in global climate models in order to simulate the strong ocean heat loss in the polar regions, thereby confirming the results of Condron and Renfrew (2013) but now based on a fully coupled global model. In addition, we show how polar lows modulate the sea ice cover, forming leads and polynyas. This heat loss is directly relevant to the formation of dense water, such as DSOW, along the sea ice margin or the direct cooling of the boundary current in the Labrador Sea. In addition, heat loss from polynyas produces new ice, resulting in brine-enriched shelf water. Capturing PLs and their effects on the ocean and sea ice requires kilometer-scale resolution in all components, namely the atmosphere, ocean, and sea ice. If mesoscale polar lows and kinematic features in the sea ice are not resolved in climate models, heat loss and dense water formation in (sub)polar regions will be underestimated.

Appendix A Water mass transformation in the Iceland Sea

In the Iceland Sea, dense water ($\geq 27.8\,\mathrm{kg\,m^{-3}}$) contributing to the Denmark Strait Overflow Water (DSOW) forms near the sea ice edge. An analysis of WMT for two density classes ($27.85 \pm 0.05\,\mathrm{kg\,m^{-3}}$ and $27.95 \pm 0.05\,\mathrm{kg\,m^{-3}}$) shows that during the studied PL, dense water of the first class forms, but not of the second class. Whereas around the 15. February 2020, also water of density $27.90\,\mathrm{kg\,m^{-3}}$) to $28.0 \pm 0.05\,\mathrm{kg\,m^{-3}}$) forms. This denser water results from a persistent heat loss that is caused by a complex interaction of polar mesoscale cyclones that sustain advection of cold polar air from over the sea ice over the Iceland Sea.

The WMT in the Iceland Sea is mainly depending on a strong temperature gradient of the sea surface temperature (SST) and the temperature in the atmospheric boundary layer, with a strong wind speed directed off the sea ice in a cold air outbreak (Fig. A2).

Code and data availability

The ICON2.5 simulation was performed by Hohenegger et al. (2023) and the source code can be retrieved from (Hohenegger, 2022). The ICON model is available to individuals under licenses (`https://mpimet.mpg.de/en/science/modeling-with-icon/code-availability`) [last accessed April 12 2023] and can be obtained following this instruction `https://code.mpimet.mpg.de/projects/iconpublic/wiki/Instructions_to_obtain_the_ICON_model_code_with_a_personal_non-commercial_research_license` [last accessed April 12 2023]. By downloading the ICON source code, the user accepts the licence agreement. For OSI SAF version 3 (OSI-450a) we acknowledge the EUMETSAT Ocean and Sea Ice Satellite Application Facility. Global sea ice concentration [interim] climate data record 1978-2020 [2021-2022]. Norwegian and Danish Meteorolog-

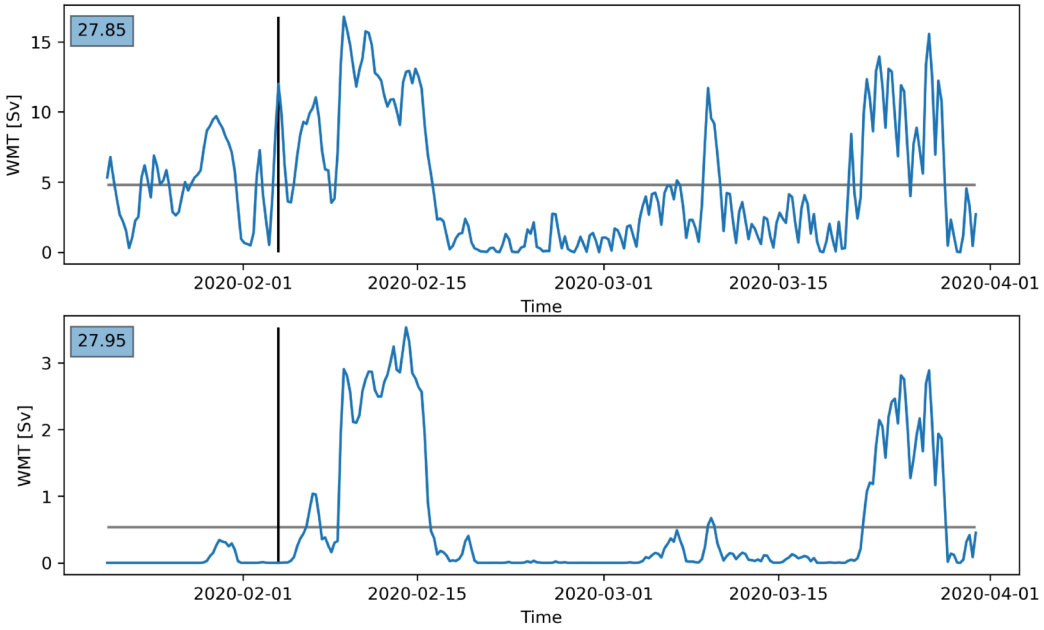

Figure A1. ICON2.5 6-hourly time series averaged over the Iceland Sea (black box in Fig. 5) from 20 January to 31 March 2020 showing water mass transformation (WMT) of the density class (a) 27.85 $\pm$ 0.05 kg m^{-3} and (b) 27.95 $\pm$ 0.05 kg m^{-3}. The grey horizontal line marks the temporal mean WMT over the entire simulation period (20 January to 31 March 2020) and the black vertical line marks the 3 February when the cold air outbreak from the studied PL was strongest over the Iceland Sea.

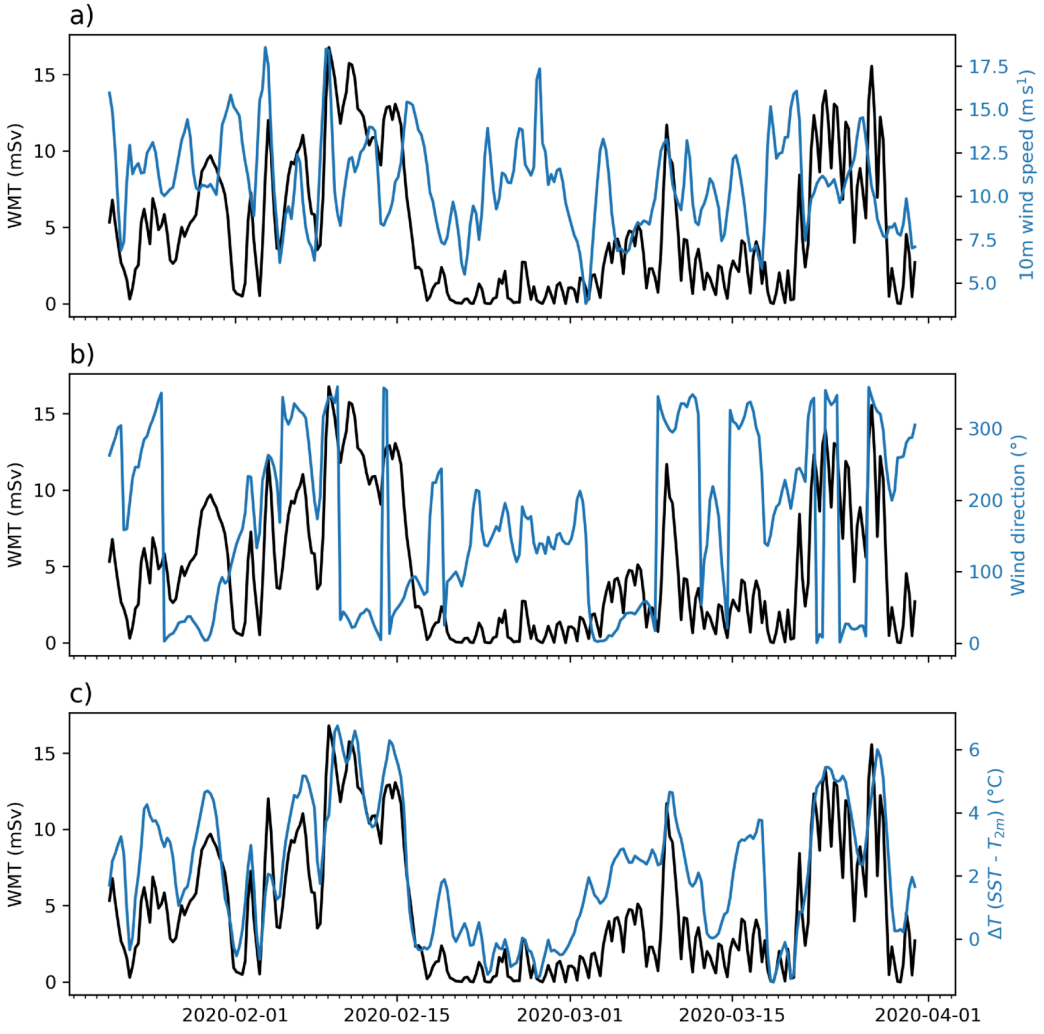

Figure A2. ICON2.5 6-hourly time series averaged over the Iceland Sea (black box in Fig. 5) from 20 January to 31 March 2020 showing water mass transformation (WMT) and (a) 10 m wind speed, (b) wind direction at 10 m height, and (c) the gradient of the sea surface temperature (SST) and the 2 m temperature (T_{2m}).

ical Institutes. Available from osisaf.met.no., doi.org/10.15770/EUM_SAF_OSI_0013 [EUM_SAF_OSI_0014] [last accessed March 15 2023]. All intellectual property rights of the OSI SAF products belong to EUMETSAT. The use of these products is granted to every interested user, free of charge. If you wish to use these products, EUMETSAT copyright credit must be shown by displaying the words "copyright (year) EUMETSAT" on each of the products used. Primary data to reproduce the figures and analysis of the paper can be retrieved for scripts from Gutjahr and Mehlmann (2023b) and for data from Gutjahr and Mehlmann (2023a).

Acknowledgments

This work is funded by the European Union as part of the EPOC project (Explaining and Predicting the Ocean Conveyor) under call HORIZON-CL6-2021-CLIMATE01. Views and opinions expressed are however those of the author(s) only and do not necessarily reflect those of the European Union. Neither the European Union nor the granting authority can be held responsible for them. C. Mehlmann is funded by the Deutsche Forschungsgemeinschaft (DFG, German Research Foundation) - Project number 463061012. The simulation was produced by the nextGEMS project (https://nextgems-h2020.eu), which is funded through the European Union's Horizon 2020 research and innovation program under the grant No - 101003470. We thank Jürgen Bader (MPI-M) for constructive comments on the manuscript. Data management was provided by the Deutsches Klimarechenzentrum (DKRZ) and supported through the projects ESiWACE and ESiWACE2. The projects ESiWACE and ESiWACE2 have received funding from the European Union's Horizon 2020 research and innovation program under grant agreements No 675191 and 823988. This work used resources of the Deutsches Klimarechenzentrum (DKRZ) granted by its Scientific Steering Committee (WLA) under project IDs bm1313 and mh0033. Thanks to ICDC, CEN, University of Hamburg for data support. All plotting and computations were done with python version 3.10.10 (https://www.python.org/).

References

Baldauf, M., Seifert, A., Förstner, J., Majewski, D., Raschendorfer, M., & Reinhardt, T. (2011). Operational Convective-Scale Numerical Weather Prediction with the COSMO Model: Description and Sensitivities. *Monthly Weather Review*, *139*(12), 3887–3905. doi: https://doi.org/10.1175/MWR-D-10-05013.1

Blanke, B., & Delecluse, P. (1993). Variability of the Tropical Atlantic Ocean Simulated by a General Circulation Model with Two Different Mixed-Layer Physics. *Journal of Physical Oceanography*, *23*(7), 1363–1388. doi: 10.1175/1520-0485(1993)023⟨1363:VOTTAO⟩2.0.CO;2

Bourke, R. H., Paquette, R. G., & Blythe, R. F. (1992). The Jan Mayen Current of the Greenland Sea. *Journal of Geophysical Research: Oceans*, *97*(C5), 7241–7250. doi: https://doi.org/10.1029/92JC00150

Brakstad, A., Gebbie, G., Våge, K., Jeansson, E., & Ólafsdóttir, S. R. (2023). Formation and pathways of dense water in the Nordic Seas based on a regional inversion. *Progress in Oceanography*, *212*, 102981. doi: https://doi.org/10.1016/j.pocean.2023.102981

Bresson, H., Hodges, K. I., Shaffrey, L. C., Zappa, G., & Schiemann, R. (2022). The Response of Northern Hemisphere Polar Lows to Climate Change in a 25 km High-Resolution Global Climate Model. *Journal of Geophysical Research: Atmospheres*, *127*(4), e2021JD035610. (e2021JD035610 2021JD035610) doi: https://doi.org/10.1029/2021JD035610

Buckley, M. W., & Marshall, J. (2016). Observations, inferences, and mechanisms of the Atlantic Meridional Overturning Circulation: A review. *Reviews of Geophysics*, *54*(1), 5–63. doi: https://doi.org/10.1002/2015RG000493

Chafik, L., & Rossby, T. (2019). Volume, Heat, and Freshwater Divergences in

the Subpolar North Atlantic Suggest the Nordic Seas as Key to the State of the Meridional Overturning Circulation. *Geophysical Research Letters*, *46*, 4799–4808. doi: 10.1029/2019GL082110

Cheng, Z., Pang, X., Zhao, X., & Tan, C. (2017). Spatio-Temporal Variability and Model Parameter Sensitivity Analysis of Ice Production in Ross Ice Shelf Polynya from 2003 to 2015. *Remote Sensing*, *9*(9). doi: 10.3390/rs9090934

Condron, A., & Renfrew, I. A. (2013). The impact of polar mesoscale storms on northeast Atlantic Ocean circulation. *Nature Geosci.*, *6*, 34–37. doi: 10.1038/ngeo1661

Cornish, S. B., Johnson, H. L., Mallett, R. D. C., Dörr, J., Kostov, Y., & Richards, A. E. (2022). Rise and fall of sea ice production in the Arctic Ocean's ice factories. *Nature Communications*, *13*, 7800. doi: 10.1038/s41467-022-34785-6

Danilov, S., Wang, Q., Timmermann, R., Iakovlev, N., Sidorenko, D., Kimmritz, M., ... Schröter, J. (2015). Finite-Element Sea Ice Model (FESIM), version 2. *Geoscientific Model Development*, *8*(6), 1747–1761. doi: 10.5194/gmd-8-1747-2015

Davy, R., & Outten, S. (2020). The arctic surface climate in cmip6: Status and developments since cmip5. *Journal of Climate*, *33*(18), 8047 - 8068. doi: https://doi.org/10.1175/JCLI-D-19-0990.1

Dickson, R., & Brown, J. (1994). The production of North Atlantic deep water: source rates and pathways. *J. Geophys. Res.*, *99*, 12319 - 12341. doi: https://doi.org/10.1175/JCLI3885.1

Doyle, J. D., & Shapiro, M. A. (1999). Flow response to large-scale topography: the Greenland tip jet. *Tellus A*, *51*, 728–748.

Drüe, C., & Heinemann, G. (2001). Airborne Investigation Of Arctic Boundary-Layer Fronts Over The Marginal Ice Zone Of The Davis Strait. *Boundary-Layer Meteorology*, *101*, 261–292. doi: https://doi.org/10.1023/A:1019223513815

Foukal, N. P., Gelderloos, R., & Pickart, R. S. (2020). A continuous pathway for fresh water along the East Greenland shelf. *Science Advances*, *6*(43), eabc4254. doi: 10.1126/sciadv.abc4254

Føre, I., Kristjánsson, J. E., Kolstad, E. W., Bracegirdle, T. J., Saetra, Ø., & Røsting, B. (2012). A 'hurricane-like' polar low fuelled by sensible heat flux: high-resolution numerical simulations. *Quarterly Journal of the Royal Meteorological Society*, *138*(666), 1308–1324. doi: https://doi.org/10.1002/qj.1876

Gaspar, P., Grégoris, Y., & Lefevre, J.-M. (1990). A simple eddy kinetic energy model for simulations of the oceanic vertical mixing: Tests at station Papa and long-term upper ocean study site. *J. Geophys. Res. Oceans*, *95*(C9), 16179–16193. doi: 10.1029/JC095iC09p16179

Giorgetta, M. A., Brokopf, R., Crueger, T., Esch, M., Fiedler, S., Helmert, J., ... Stevens, B. (2018). ICON-A, the Atmosphere Component of the ICON Earth System Model: I. Model Description. *Journal of Advances in Modeling Earth Systems*, *10*, 1613–1637. doi: 10.1029/2017MS001242

Graham, R. M., Itkin, P., Meyer, A., Sundfjord, A., Spreen, G., Smedsrud, L. H., ... Granskog, M. A. (2019). Winter storms accelerate the demise of sea ice in the Atlantic sector of the Arctic Ocean. *Scientific Reports*, *9*, 2045–2322. doi: 10.1038/s41598-019-45574-5

Groeskamp, S., Griffies, S. M., Iudicone, D., Marsh, R., Nurser, A. J. G., & Zika, J. D. (2019). The Water Mass Transformation Framework for Ocean Physics and Biogeochemistry. *Annual Review of Marine Science*, *11*, 271–305. doi: 10.1146/annurev-marine-010318-095421

Gutjahr, O., & Heinemann, G. (2018). A model-based comparison of extreme winds in the Arctic and around Greenland. *Int. J. Climatol.*, *38*, 5272–5292. doi: 10.1002/joc.5729

Gutjahr, O., Heinemann, G., Preußer, A., Willmes, S., & Drüe, C. (2016). Quantifi-

cation of ice production in Laptev Sea polynyas and its sensitivity to thin-ice parameterizations in a regional climate model. *The Cryosphere*, *10*(6), 2999–3019. doi: 10.5194/tc-10-2999-2016

Gutjahr, O., Jungclaus, J. H., Brüggemann, N., Haak, H., & Marotzke, J. (2022). Air-sea interactions and water mass transformation during a katabatic storm in the Irminger Sea. *Journal of Geophysical Research: Oceans*, *127*, e2021JC018075. doi: 10.1029/2021JC018075

Gutjahr, O., & Mehlmann, C. (2023a). *Polar lows and their effects on sea ice and the upper ocean in the Iceland, Greenland and Labrador Seas - Icon-Sapphire 2.5 km data.* World Data Center for Climate (WDCC) at DKRZ. Retrieved from `https://www.wdc-climate.de/ui/entry?acronym=DKRZ_LTA_1313_ds00001` (last access: 20.06.2023)

Gutjahr, O., & Mehlmann, C. (2023b). *Polar lows and their effects on sea ice and the upper ocean in the Iceland, Greenland and Labrador Seas - Scripts.* Retrieved from `https://hdl.handle.net/21.11116/0000-000D-4D7D-2` (last access: 23.06.2023)

Hallerstig, M., Magnusson, L., Kolstad, E. W., & Mayer, S. (2021). How grid-spacing and convection representation affected the wind speed forecasts of four polar lows. *Quarterly Journal of the Royal Meteorological Society*, *147*(734), 150-165. doi: https://doi.org/10.1002/qj.3911

Harden, B. E., Renfrew, I. A., & Petersen, G. N. (2015). Meteorological buoy observations from the central Iceland Sea. *Journal of Geophysical Research: Atmospheres*, *120*(8), 3199-3208. doi: https://doi.org/10.1002/2014JD022584

Heinemann, G. (1996). On the Development of Wintertime Meso-Scale Cyclones near the Sea Ice Front in the Arctic and Antarctic. *Global Atmos.-Ocean Syst.*, *4*, 89–121.

Heinemann, G., & Claud, C. (1997). Report of a Workshop on Theoretical and Observational Studies of Polar Lows" of the European Geophysical Society Polar Lows Working Group". *Bulletin of the American Meteorological Society*, *78*(11), 2643 - 2658. doi: 10.1175/1520-0477-78.11.2643

Heuzé, C., Zanowski, H., Karam, S., & Muilwijk, M. (2023). The deep arctic ocean and fram strait in cmip6 models. *Journal of Climate*, *36*(8), 2551 - 2584. doi: https://doi.org/10.1175/JCLI-D-22-0194.1

Hewitt, H., Fox-Kemper, B., Pearson, B., Roberts, M., & D., K. (2022). The small scales of the ocean may hold the key to surprises. *Nature Climate Change*, *12*, 496–499. doi: 10.1038/s41558-022-01386-6

Hohenegger, C. (2022). *Code for "ICON-Sapphire: simulating the components of the Earth System and their interactions at kilometer and subkilometer scales".* Edmond. Retrieved from `https://doi.org/10.17617/3.1XTSR6` doi: 10.17617/3.1XTSR6

Hohenegger, C., Korn, P., Linardakis, L., Redler, R., Schnur, R., Adamidis, P., ... Stevens, B. (2023). Icon-sapphire: simulating the components of the earth system and their interactions at kilometer and subkilometer scales. *Geoscientific Model Development*, *16*(2), 779–811. doi: 10.5194/gmd-16-779-2023

Hunke, E. C., & Dukowicz, J. K. (1997). An Elastic–Viscous–Plastic Model for Sea Ice Dynamics. *Journal of Physical Oceanography*, *27*(9), 1849–1867. doi: https://doi.org/10.1175/1520-0485(1997)027⟨1849:AEVPMF⟩2.0.CO;2

Jung, T., Gordon, N. D., Bauer, P., Bromwich, D. H., Chevallier, M., Day, J. J., ... Yang, Q. (2016). Advancing polar prediction capabilities on daily to seasonal time scales. *Bulletin of the American Meteorological Society*, *97*(9), 1631 - 1647. doi: https://doi.org/10.1175/BAMS-D-14-00246.1

Jungclaus, J., Lorenz, S., Schmidt, H., Brovkin, V., Brüggemann, N., Chegini, F., ... Claussen, M. (2022). The ICON Earth System Model Version 1.0. *Journal of Advances in Modeling Earth Systems*, *14*, e2021MS002813. doi: https://doi.org/10.1029/2021MS002813

Klein, T., & Heinemann, G. (2002). Interaction of katabatic winds and mesocyclones near the eastern coast of Greenland. *Meteorol. Appl.*, *9*, 407–422. doi: 10.1017/S1350482702004036

Kolstad, E. W. (2015). Extreme small-scale wind episodes over the Barents Sea: When, where and why? *Clim. Dynam.*, *45*(7-8), 2137–2150. doi: 10.1007/s00382-014-2462-4

Korn, P. (2017). Formulation of an unstructured grid model for global ocean dynamics. *J. Comp. Physiol.*, *339*, 525–552. doi: 10.1016/j.jcp.2017.03.009

Korn, P., Brüggemann, N., Jungclaus, J. H., Lorenz, S. J., Gutjahr, O., Haak, H., ... Marotzke, J. (2022). ICON-O: The Ocean Component of the ICON Earth System Model—Global Simulation Characteristics and Local Telescoping Capability. *Journal of Advances in Modeling Earth Systems*, *14*(10), e2021MS002952. doi: https://doi.org/10.1029/2021MS002952

Kristjánsson, J. E., Thorsteinsson, S., Kolstad, E. W., & Blechschmidt, A.-M. (2011). Orographic influence of east Greenland on a polar low over the Denmark Strait. *Quarterly Journal of the Meteorological Society*, *137*, 1773–1789. doi: 10.1002/qj.831

Lavergne, T., Sørensen, A. M., Kern, S., Tonboe, R., Notz, D., Aaboe, S., ... Pedersen, L. T. (2019). Version 2 of the EUMETSAT OSI SAF and ESA CCI sea-ice concentration climate data records. *The Cryosphere*, *13*(1), 49–78. doi: 10.5194/tc-13-49-2019

Lilly, D. K. (1962). On the numerical simulation of buoyant convection. *Tellus*, *14*(2), 148–172. doi: https://doi.org/10.1111/j.2153-3490.1962.tb00128.x

Louis, J.-F. (1979). A parametric model of vertical eddy fluxes in the atmosphere. *Boundary-Layer Meteorol*, *17*, 187–202. doi: https://doi.org/10.1007/BF00117978

Lozier, M. S., Li, F., Bacon, S., Bahr, F., Bower, A. S., Cunningham, S. A., ... Zhao, J. (2019). A sea change in our view of overturning in the subpolar North Atlantic. *Science*, *363*(6426), 516–521. doi: 10.1126/science.aau6592

Mc Innes, H., Kristiansen, J., Kristjánsson, J. E., & Schyberg, H. (2011). The role of horizontal resolution for polar low simulations. *Q. J. R. Meteorol. Soc.*, *137*(660), 1674–1687. doi: 10.1002/qj.849

Moore, G. W. K., Våge, K., Renfrew, I. A., & Pickart, R. S. (2022). Sea-ice retreat suggests re-organization of water mass transformation in the Nordic and Barents Seas. *Nat. Commun.*, *13*(67), 1–8. doi: 10.1038/s41467-021-27641-6

Morales Maqueda, M. A., Willmott, A. J., & Biggs, N. R. T. (2004). Polynya Dynamics: a Review of Observations and Modeling. *Reviews of Geophysics*, *42*(1). doi: https://doi.org/10.1029/2002RG000116

Moreno-Ibáñez, M., Laprise, R., & Gachon, P. (2021). Recent advances in polar low research: current knowledge, challenges and future perspectives. *Tellus A: Dynamic Meteorology and Oceanography*, *73*(1), 1–31. doi: 10.1080/16000870.2021.1890412

Orlanski, I. (1975). A Rational Subdivision of Scales for Atmospheric Processes. *Bulletin of the American Meteorological Society*, *56*(5), 527–530.

Papritz, L., & Spengler, T. (2017). A Lagrangian Climatology of Wintertime Cold Air Outbreaks in the Irminger and Nordic Seas and Their Role in Shaping Air–Sea Heat Fluxes. *Journal of Climate*, *30*(8), 2717 - 2737. doi: https://doi.org/10.1175/JCLI-D-16-0605.1

Pedersen, J. B. T., Kaufmann, L. H., Kroon, A., & Jakobsen, B. H. (2010). The Northeast Greenland Sirius Water Polynya dynamics and variability inferred from satellite imagery. *Geografisk Tidsskrift-Danish Journal of Geography*, *110*(2), 131–142. doi: 10.1080/00167223.2010.10669503

Petit, T., Lozier, M. S., Josey, S. A., & Cunningham, S. A. (2020). Atlantic Deep Water Formation Occurs Primarily in the Iceland Basin and Irminger Sea by Local Buoycancy Forcing. *Geophys. Res. Lett.*, *47*, e2020GL091028. doi:

10.1029/2020GL091028

Pickart, R. S., Spall, M. A., Ribergaard, M. H., Moore, G. W. K., & Milliff, R. F. (2003). Deep convection in the Irminger Sea forced by the Greenland tip jet. *Nature*, *424*(6945), 152–156. doi: 10.1038/nature01729

Pincus, R., Mlawer, E. J., & Delamere, J. S. (2019). Balancing Accuracy, Efficiency, and Flexibility in Radiation Calculations for Dynamical Models. *Journal of Advances in Modeling Earth Systems*, *11*(10), 3074-3089. doi: https://doi.org/10.1029/2019MS001621

Rasmussen, E. A., & Turner, J. (2003). *Polar Lows: Mesoscale Weather Systems in the Polar Regions*. Cambridge University Press. doi: 10.1017/CBO9780511524974

Reick, H., Gayler, V., Goll, D., Hagemann, S., Heidkamp, M., Nabel, J. E. M. S., ... Wilkenskjeld, S. (2021). JSBACH 3 - The land component of the MPI Earth System Model: documentation of version 3.2. *Berichte zur Erdsystemforschung*, *240*. doi: 10.17617/2.3279802

Renfrew, I. A., Huang, J., Semper, S., Barrell, C., Terpstra, A., Pickart, R. S., ... Weiss, A. (2023). Coupled atmosphere–ocean observations of a cold-air outbreak and its impact on the Iceland Sea. *Quarterly Journal of the Royal Meteorological Society*, *149*(751), 472-493. doi: https://doi.org/10.1002/qj.4418

Renfrew, I. A., Pickart, R. S., Våge, K., Moore, G. W. K., Bracegirdle, T. J., Elvidge, A. D., ... Zhou, S. (2019). The iceland greenland seas project. *Bulletin of the American Meteorological Society*, *100*(9), 1795 - 1817. doi: https://doi.org/10.1175/BAMS-D-18-0217.1

Semtner, A. J. (1976). A Model for the Thermodynamic Growth of Sea Ice in Numerical Investigations of Climate. *Journal of Physical Oceanography*, *6*(3), 379–389. doi: https://doi.org/10.1175/1520-0485(1976)006⟨0379:AMFTTG⟩2.0.CO;2

Skogseth, R., Haugan, P. M., & Haarpaintner, J. (2004). Ice and brine production in Storfjorden from four winters of satellite and in situ observations and modeling. *Journal of Geophysical Research: Oceans*, *109*(C10). doi: https://doi.org/10.1029/2004JC002384

Skogseth, R., Smedsrud, L. H., Nilsen, F., & Fer, I. (2008). Observations of hydrography and downflow of brine-enriched shelf water in the Storfjorden polynya, Svalbard. *Journal of Geophysical Research: Oceans*, *113*(C8). doi: https://doi.org/10.1029/2007JC004452

Smagorinsky, J. (1963). General circulation experiments with the primitive equations. *Monthly Weather Review*, *91*(3), 99–164. doi: https://doi.org/10.1175/1520-0493(1963)091⟨0099:GCEWTP⟩2.3.CO;2

Smedsrud, L. H., Muilwijk, M., Brakstad, A., Madonna, E., Lauvset, S. K., Spensberger, C., ... Årthun, M. (2022). Nordic Seas Heat Loss, Atlantic Inflow, and Arctic Sea Ice Cover Over the Last Century. *Reviews of Geophysics*, *60*(1), e2020RG000725. (e2020RG000725 2020RG000725) doi: https://doi.org/10.1029/2020RG000725

Spall, M. A., Almansi, M., Huang, J., Haine, T. W., & Pickart, R. S. (2021). Lateral redistribution of heat and salt in the nordic seas. *Progress in Oceanography*, *196*, 102609. doi: https://doi.org/10.1016/j.pocean.2021.102609

Speer, K., & Tziperman, E. (1992). Rates of water mass formation in the North Atlantic ocean. *J. Phys. Oceanogr.*, *22*, 93–104. doi: 10.1175/1520-0485(1992)022⟨0093:ROWMFI⟩2.0.CO;2

Spensberger, C., & Spengler, T. (2021). Sensitivity of air-sea heat exchange in cold-air outbreaks to model resolution and sea-ice distribution. *Journal of Geophysical Research: Atmospheres*, *126*(5), e2020JD033610. (e2020JD033610 2020JD033610) doi: https://doi.org/10.1029/2020JD033610

Steele, M., Morley, R., & Ermold, W. (2001). PHC: A Global Ocean Hydrography with a High-Quality Arctic Ocean. *Journal of Climate*, *14*(9), 2079–2087. doi:

https://doi.org/10.1175/1520-0442(2001)014⟨2079:PAGOHW⟩2.0.CO;2

Steffen, E. L., & D'Asaro, E. A. (2002). Deep Convection in the Labrador Sea as Observed by Lagrangian Floats. *Journal of Physical Oceanography*, *32*(2), 475–492. doi: https://doi.org/10.1175/1520-0485(2002)032⟨0475:DCITLS⟩2.0.CO;2

Stevens, B., Satoh, M., Auger, L., Biercamp, J., Bretherton, C., Chen, X., ... Zhou, L. (2019). DYAMOND: The DYnamics of the Atmospheric circulation Modeled On Non-hydrostatic Domains. *Progress in Earth and Planetary Science*, *6*(61). doi: 10.1186/s40645-019-0304-z

Svingen, K., Brakstad, A., Våge, K., von Appen, W.-J., & Papritz, L. (2023). The Impact of Cold-Air Outbreaks and Oceanic Lateral Fluxes on Dense-Water Formation in the Greenland Sea from a 10-Year Moored Record (1999–2009). *Journal of Physical Oceanography*, *53*(6), 1499 - 1517. doi: https://doi.org/10.1175/JPO-D-22-0160.1

Terpstra, A., Renfrew, I. A., & Sergeev, D. E. (2021). Characteristics of Cold-Air Outbreak Events and Associated Polar Mesoscale Cyclogenesis over the North Atlantic Region. *Journal of Climate*, *34*(11), 4567–4584. doi: https://doi.org/10.1175/JCLI-D-20-0595.1

UNESCO. (1981). The practical salinity scale 1978 and the international equation of state of seawater 1980. *UNESCO technical papers in marine science 36*.

Våge, K., Moore, G., Jónsson, S., & Valdimarsson, H. (2015). Water mass transformation in the Iceland Sea. *Deep Sea Research Part I: Oceanographic Research Papers*, *101*, 98–109. doi: https://doi.org/10.1016/j.dsr.2015.04.001

Våge, K., Papritz, L., Håvik, L., Spall, M. A., & Moore, G. (2018). Ocean convection linked to the recent ice edge retreat along east Greenland. *Nature Communications*, *9*, 1287. doi: https://doi.org/10.1038/s41467-018-03468-6

Våge, K., Semper, S., Valdimarsson, H., Jónsson, S., Pickart, R. S., & Moore, G. (2022). Water mass transformation in the Iceland Sea: Contrasting two winters separated by four decades. *Deep Sea Research Part I: Oceanographic Research Papers*, *186*, 103824. doi: https://doi.org/10.1016/j.dsr.2022.103824

Wang, Q., Danilov, S., Jung, T., Kaleschke, L., & Wernecke, A. (2016). Sea ice leads in the arctic ocean: Model assessment, interannual variability and trends. *Geophysical Research Letters*, *43*(13), 7019-7027. doi: https://doi.org/10.1002/2016GL068696

Wu, L. (2021). Effect of atmosphere-wave-ocean/ice interactions on a polar low simulation over the Barents Sea. *Atmospheric Research*, *248*, 105183. doi: https://doi.org/10.1016/j.atmosres.2020.105183

Zhou, L., Heuzé, C., & Mohrmann, M. (2023). Sea Ice Production in the 2016 and 2017 Maud Rise Polynyas. *Journal of Geophysical Research: Oceans*, *128*(2), e2022JC019148. (e2022JC019148 2022JC019148) doi: https://doi.org/10.1029/2022JC019148